A Statistical Study of Short-period Decayless Oscillations of Coronal Loops in an Active Region

Dong Li[1] and David Long[2]

[1] *Purple Mountain Observatory, Chinese Academy of Sciences, Nanjing 210023, PR China*
[2] *UCL-Mullard Space Science Laboratory, Holmbury House, Holmbury St. Mary, Dorking, Surrey, RH5 6NT, UK*

ABSTRACT

Coronal loop oscillations are common phenomena in the solar corona, which are often classified as decaying and decayless oscillations. Using the high-resolution observation measured by the Extreme Ultraviolet Imager (EUI) onboard the Solar Orbiter, we statistical investigate small-scale transverse oscillations with short periods (<200 s) of coronal loops in an active region, i.e., NOAA 12965. A total of 111 coronal loops are identified in EUI 174 Å images, and they all reveal transverse oscillations without any significant decaying, regarding as decayless oscillations. Oscillatory periods are measured from ∼11 s to ∼185 s, with a median period of 40 s. Thus, they are also termed as short-period oscillations. The corresponding loop lengths are measured from ∼10.5 Mm to ∼30.2 Mm, and a strong dependence of oscillatory periods on loop lengths is established, indicating that the short-period oscillations are standing kink-mode waves in nature. Based on the coronal seismology, kink speeds are measured to ∼330−1910 km s^{-1}, and magnetic field strengths in coronal loops are estimated to about 4.1−25.2 G, while the energy flux carried by decayless kink oscillations lies in the range from roughly 7 W m^{-2} to 9220 W m^{-2}. Our estimations suggest that the wave energy carried by short-period decayless kink oscillations can not support the coronal heating in the active region.

Subject headings: Solar coronal loops — Solar ultraviolet emission — Solar oscillations — Magnetohydrodynamics — Solar coronal seismology

1. Introduction

Coronal loops are basic building magnetic structures in solar outer atmospheres, which are frequently detected in active regions (ARs), coronal holes, and quiet-Sun regions (Reale 2014; Mac Cormack et al. 2022). The observed lengths of coronal loops are ranging from several hundreds

Correspondence should be sent to: lidong@pmo.ac.cn

kilometers (km) to a few hundreds megameters (Mm) in the solar corona, and the temperature of plasma loops is in the magnitude order of mega-Kelvin (MK) (Aschwanden & Boerner 2011; Peter et al. 2013; Gupta et al. 2019). Thus, the coronal loop can be easily observed in wavebands of extreme-ultraviolet (EUV) and Soft X-ray (SXR). Observations find that a typical coronal loop-like structure generally following the magnetic field line, for instance, the open coronal structure has only one apparent polarity and could extend radially along the magnetic field line, while the closed coronal loop connects to double footpoints that are rooted in positive and negative polarities, respectively (e.g., Watko & Klimchuk 2000; Feng et al. 2007; Peter & Bingert 2012; Li et al. 2020a). Therefore, coronal loops are thought to be associated with the mass supply and plasma heating in the solar corona, and would help us to understand the coronal heating problem better (e.g., Klimchuk 2015; Li et al. 2019; Antolin & Froment 2022).

Coronal loops are highly dynamic. The prominent dynamic is the transverse oscillation, which was first detected by the Transition Region and Coronal Explorer (TRACE; Handy et al. 1999) spacecraft (see, Aschwanden et al. 1999; Nakariakov et al. 1999). These observed transverse oscillations are usually decaying rapidly, namely they can only persist over a few wave periods (Goddard et al. 2016; Su et al. 2018; Nechaeva et al. 2019). In the Solar Dynamics Observatory (SDO; Pesnell et al. 2012) era, the loop oscillations without significant damping, regarded as decayless oscillations, are found to be a common phenomenon in the solar corona (e.g., Wang et al. 2012; Anfinogentov et al. 2013, 2015). Transverse decayless oscillations are also detected in coronal bright points (Gao et al. 2022), solar flares (Tian et al. 2016; Li et al. 2018a), and prominence threads (Díaz et al. 2001; Ning et al. 2009; Li et al. 2018b), since they all consist of loop- or thread-like structures that could be regarded as thin magnetic flux tubes in the corona (Goossens et al. 2013). These observations further confirm that transverse decayless oscillations are omnipresent in solar atmospheres (Okamoto et al. 2007; Tian et al. 2012; Li et al. 2022), and thus could provide persistent energy input which compensates energy losses in the solar chromosphere and corona (e.g., Morton et al. 2012; Tian et al. 2014; Van Doorsselaere et al. 2020). Decaying oscillations are often excited by external solar eruptions, such as solar flares, coronal jets and rains, EUV waves, reconnection outflows, or flux-rope eruptions, and so on (e.g., Antolin & Verwichte 2011; Zimovets & Nakariakov 2015; Shen et al. 2017, 2018a; Reeves et al. 2020; Zhang et al. 2020, 2022). Their apparent displacement amplitudes are much larger than 1 Mm, while their decaying time is about several oscillatory periods and decreases with oscillating amplitudes (Goddard et al. 2016; Nechaeva et al. 2019; Zhang 2020; Ning et al. 2022). Conversely, decayless oscillations often have small displacement amplitudes, i.e., $<$1 Mm, which are always shorter than the minor radius of oscillating loops (Anfinogentov et al. 2015). The driving mechanism of decayless oscillations is still debated (Mandal et al. 2022), such as the magnetic arcade model (Hindman & Jain 2014), the Kelvin-Helmholtz (KH) vortices model (Antolin et al. 2016), the self-oscillation model (Nakariakov et al. 2016), the footpoint harmonic-driver model (Karampelas et al. 2017), the steady-flow driver model (Karampelas & Van Doorsselaere 2020), and the random-motion driver model (Afanasyev et al. 2020; Ruderman & Petrukhin 2021), etc. Recently, the decayless transverse oscillations of coronal loops were found to be induced by a solar flare, which just increases oscillatory amplitudes

(Mandal et al. 2021).

Transverse oscillations of coronal loops are often interpreted as magnetohydrodynamic (MHD) waves in the solar corona, including decaying and decayless oscillations (see, Nakariakov & Verwichte 2005; Nakariakov & Kolotkov 2020, and references therein). In observations of transverse oscillations, one of the most commonly measured MHD modes is termed as 'kink oscillations', which are always perpendicular to the bulk parameters of oscillating loops, nonaxisymmetric, and nearly incompressive in the long-wavelength regime (Nakariakov et al. 2021, 2022; Lopin 2022). The standing kink-mode oscillation may be triggered by an impulsive energy-release process, i.e., an erupted event in the low corona (Nakariakov et al. 2021). The oscillatory period is found to increase linearly with the length of plasma loops (Anfinogentov et al. 2015; Goddard et al. 2016; Zhong et al. 2022). Another type of transverse oscillations in plasma loops is the fast sausage-mode oscillations. Unlike kink waves, they are essentially compressive and strongly dispersive. Wave motions are also perpendicular to the loop axis, but axisymmetric, i.e., expanding-contracting of the loop cross section instead of 'kinking' of the loop axis (Chen et al. 2015; Sadeghi & Karami 2019; Li et al. 2020, 2021; Guo et al. 2021). For the coronal conditions expected periods of sausage oscillations are about 10 seconds and below. SDO/AIA and previous generations of EUV solar telescopes do not have high enough observational cadence to detect such short-period oscillations. Indeed, imaging observations of sausage oscillations are rare. Nakariakov et al. (2003) discussed global sausage oscillations, meaning fundamental-mode waves, when the wavelength is equal to the doubled length of the oscillating loop, and stated that they can only exist in thicker and denser plasma loops. While the higher harmonics and local sausage oscillations can also appear in thin and less dense loops. The global fast sausage-mode oscillation is seen in a hotter flaring loop with spectroscopic observations (Tian et al. 2016), while the standing slow and fast sausage waves are simultaneously observed in a flare loop by using the time series in the Lyα line emission (Van Doorsselaere et al. 2011). Slow magnetoacoustic waves, also regarded as 'SUMER' oscillations, are often used to interpret coronal loop oscillations (Ofman & Wang 2002; Wang 2011; Wang et al. 2021). The slow magnetoacoustic-mode oscillation is a longitudinal-mode wave, which is predominantly the parallel flow along plasma loops and always decaying rapidly and often has a longer oscillatory period (Kumar et al. 2013; Yuan et al. 2015; Kolotkov et al. 2019; Nakariakov et al. 2019). The study of MHD oscillations in coronal loops becomes a topic of particular interest, since it is an important tool for remotely inferring plasma parameters and estimating magnetic field strengths in the solar corona and chromosphere, named as 'MHD coronal seismology' (De Moortel & Nakariakov 2012; Yuan & Van Doorsselaere 2016a,b; Yuan et al. 2016; Long et al. 2017; Anfinogentov et al. 2022; Li et al. 2022; Pascoe et al. 2022). Moreover, they can allow us to global map the coronal magnetic field (e.g., Yang et al. 2020a,b).

Transverse oscillations are usually observed as the spatial displacement oscillations of plasma loops in EUV and SXR image sequences (Aschwanden et al. 1999; Nakariakov et al. 1999; Anfinogentov et al. 2013; Duckenfield et al. 2018; Li et al. 2020b; Zhang 2020). They are also detected as Doppler velocity oscillations of magnetic loops in EUV spectral lines when the slit happens to cross the plasma

loop (Mariska & Muglach 2010; Zhou et al. 2016; Li et al. 2017), which can effectively avoid the saturation effect of imaging observations. Imaging observations showed that the oscillatory period in coronal loops was ranging from a few minutes to several tens minutes (Anfinogentov et al. 2015; Shen et al. 2018; Duckenfield et al. 2019; Nechaeva et al. 2019; Goddard & Nisticò 2020; Zhang et al. 2022). On the other hand, spectroscopic observations found that the oscillatory period in hot flaring loops could be less than 1 minute (Tian et al. 2016; Li et al. 2018a). This is mainly because the time cadence of EUV/SXR images is a bit lower, for instance, the Atmospheric Imaging Assembly (AIA; Lemen et al. 2012) on board SDO takes EUV images at a cadence of 12 s, making it difficult to detect short-period oscillations. Now, the high-resolution telescope of the Extreme Ultraviolet Imager (EUI; Rochus et al. 2020) onboard the Solar Orbiter (SolO; Müller et al. 2020) can provide the higher spatial and temporal resolution image sequences at the wavelength of 174 Å, giving us an opportunity to investigate the small-scale transverse oscillations at short periods, i.e., <1 minute. In order to balance the strong energy losses and preserve the high temperature in the corona, it must be ongoing heated by $\sim$100$-$200 W m^{-2} for the quiet-Sun region, while it needs as high as $\sim$10^4 W m^{-2} for the active regions (Withbroe & Noyes 1977). In the past few decades, many mechanisms have been proposed to be possible candidates for the deposition of input energies, i.e., MHD waves (Van Doorsselaere et al. 2020; Shi et al. 2021). In particularly, the decayless kink-mode wave at short periods could contribute to the energy input that is required to heat the quiet corona (cf. Petrova et al. 2022). However, it is only the case study, a statistical study of decayless oscillations at short periods is still rare, especially for active region loops.

In this work, we present a statistical investigation of decayless oscillations at short periods and estimate their energy flux using the MHD coronal seismology. The article is organized as follows: Section 2 describes in detail observations and instruments used in this study, Section 3 gives details of the data reduction and MHD methods, Section 4 presents our statistical results, Section 5 offers discussions, and a brief summary is given in Section 6.

2. Observations and Instruments

The observational data sets are mainly from SolO/EUI, which contains three telescopes: two High Resolution Imagers (HRI) and one Full Sun Imager (FSI). The labeled 'HRI$_{\rm EUV}$' telescope provides local coronal images with a field of view (FOV) of about 16.8′×16.8′ at 174 Å, which is dominated by two coronal lines of Fe IX and Fe X and has a formation temperature of about 1 MK. The named 'HRI$_{\rm Ly\alpha}$' telescope provides local chromospheric images with the same FOV of $\sim$16.8′×16.8′ at 1216 Å, which is characterized by the Lyα emission of neutral hydrogen line (cf. Berghmans et al. 2021; Chen et al. 2021). The FSI telescope observes the full-disk Sun with an uniquely large FOV of about 3.8°×3.8° at wavelengths of 174 Å and 304 Å (cf. Müller et al. 2020; Mierla et al. 2022). The data sets analysed in this study were obtained on 17 March 2022. On that day, SolO was located at about 26.5° west in solar longitude from the Sun-Earth line, and the distance between the SolO and the Sun was about 0.379 AU, as shown in Figure 1. Hence, it

looked at the Sun from a different perspective, comparing with the telescopes in Earth orbit.

The Level 2 data production is downloaded from the EUI Data Release 5.0[1], and they have been pre-processed by the EUI team (i.e., EUI_PREP.PRO). We also performed a cross-correlation technique to test the image co-alignment (cf. Mandal et al. 2022). The targeted active region (AR) of NOAA12965 was observed by the $\mathrm{HRI_{EUV}}$ telescope on 17 March 2022 during 03:18:00−04:02:51 UT, as shown in Figure 2 (a). The $\mathrm{HRI_{EUV}}$ images at 174 Å were acquired with a time cadence of about 3 s and a pixel scale of ∼0.49″, corresponding to about 135 km, as listed in Table 1. The $\mathrm{HRI_{Ly\alpha}}$ images at 1216 Å were provided from 03:18:00 UT to 03:46:55 UT, the time cadence is about 5 s, and each pixel scale corresponds to about 282 km. FSI captured the full-disk images at 304 Å between 03:50:00 UT to 04:03:00 UT with a time cadence of 60 s, and every pixel scale corresponds to about 1219 km. There is a data gap for the FSI image acquisition at 174 Å, which missed our observation. It should be pointed out that the time is selected at the SolO location, which has a time difference of about 307.5 s with respect to the light travel time from the Sun to the Earth asset.

The Spectrometer/Telescope for Imaging X-rays (STIX; Krucker et al. 2020) on board SolO provides X-ray imaging spectroscopy of the Sun at a time cadence of 4 s. The energy range measured by STIX is mainly from 4 keV to 150 keV. Here, we analyzed the STIX quick-look light curves at energy ranges of 4−10 keV, 10−15 keV, and 15−25 keV, as shown in Table 1. The AR of NOAA12965 was also observed by SDO/AIA in Earth orbit from a different perspective, as shown in Figure 1. The energy spectrum and X-ray images are not used due to the lower X-ray counts. AIA is designed to measure full-disk solar images at a spatial scale of 0.6″ per pixel (corresponds to about ∼435 km) in seven EUV and two UV wavelength bands. It also provides rebinned solar images at a lower spatial scale and a longer time cadence (Lemen et al. 2012). In our study, two AIA images at wavelengths of 171 Å and 131 Å are used, and they are dominated by coronal and flare lines, such as Fe IX (∼0.6 MK), Fe VIII (∼0.4 MK) and Fe XXI (∼11 MK), respectively. The AIA 171 image has a time cadence of 12 s and a pixel scale of about 435 km, while the 131 Å image has been spatially rebinned (4×) with a time cadence of 120 s and a pixel scale of about 1740 km, as shown in Table 1.

3. Data reduction and Methods

We analyzed fine-scale coronal loops (e.g., the loop length is a few tens Mm) in the AR of NOAA 12965, as shown in Figure 2. Panel (a) presents the targeted AR at 03:18:00 UT in $\mathrm{HRI_{EUV}}$ 174 Å observed by SolO/EUI, and many groups of loop-like structures appear in the AR, including large-scale (e.g., the length order of about one hundred Mm) and fine-scale coronal loops. Those large-scale loops can also be seen in the AIA 171 image that observed the targeted AR

[1]https://doi.org/10.24414/2qfw-tr95

at a different perspective, as shown in panel (b). Here, we have corrected the time shift between SDO/AIA and SolO/EUI, i.e., 307.5 s. On the other hand, these fine-scale loops can be clearly seen in the HRI_{EUV} 174 Å image, as indicated by R1 and R2 regions. However, they are not so obvious in the AIA 171 image, largely due to its lower spatial resolution. In Figure 2 (c) and (d), we display two sub-fields corresponding to the green boxes outlined in panel (a), which clearly reveal these fine-scale coronal loops. Then, we extracted thirteen artificial slits that are almost perpendicular to coronal loops to perform the time-distance map, as indicated by the cyan lines.

3.1. Detection of short-period decayless oscillations

From the online animation, we can see that coronal loops exhibit highly dynamic, such as drifting motions, rotation movements, transverse and longitudinal oscillations. Here, we focus on the transverse oscillations of fine-scale coronal loops, particularly for the decayless oscillations with periods shorter than 200 s. Some brightest loops are not selected to avoid the saturated pixels.

In order to enhance the appearance of small-scale oscillations, a smooth window of 200 s is applied to the original map (cf. Mandal et al. 2022; Zhong et al. 2022). The smooth window is reasonable, since we are only interested in the short periods, i.e., <200 s. Figure 3 (a) plots the time-distance map after removing a smooth version along the slit S1 in Figure 2 (c), which are made from the image sequences at HRI_{EUV} 174 Å. Here, the starting point of the time-distance analysis is indicated by the green symbol of '$*$'. Totally, 13 coronal loop oscillations (the detail can be seen in the Appendix A) are found in this time-distance map, as indicated by cyan circles, which represent the central or boundary positions of oscillating loops. Generally, the loop centers are determined by Gaussian fitting (e.g., Wang et al. 2012; Zhong et al. 2022). However, it could be difficult to apply this method when a series of overlapping loop structures simultaneously appear in the time-distance map (Anfinogentov et al. 2015; Goddard et al. 2016; Gao et al. 2022). Thus, we manually identified those brightest/weakest pixels as loop centers or edges. It should be pointed out that although some coronal loops reveal oscillations, they also show strongly vortex motions, and we have to abandon them, i.e., those coronal loops in the region centered at x≈1500 s and y≈15 Mm. These thirteen coronal loops show transverse oscillations without significant decaying, which could be regarded as decayless oscillations. We also note that some coronal loop oscillations drift significantly, such as loops 6 and 13, while some others drift weakly, i.e., loops 4 and 7. Therefore, the decayless oscillation is fitted by a widely adopted function, namely, the sine function with a linear trend but without the decaying term (cf. Anfinogentov et al. 2013, 2015; Li et al. 2020b; Zhang 2020; Gao et al. 2022), as indicated by Equation 1:

$$A(t) = A_m \sin(\frac{2\pi}{P}\ t + \phi) + kt + A_0, \tag{1}$$

where A_m stands for the displacement amplitude, P is the oscillatory period, ϕ and A_0 represent the initial phase and initial position of the oscillating motion, while k is constant and denotes to

the drifting velocity of the oscillating loop in the plane-of-the-sky (e.g., Ning et al. 2009; Li et al. 2018b; Zhang et al. 2022). The fitting results are indicated by the magenta curves, and they appear to match well with the oscillatory positions of coronal loops. Using the derivative of Equation 1, the velocity amplitude (v_m) of the decayless oscillations could be derived (cf. Li et al. 2022; Petrova et al. 2022), that is, $v_m = 2\pi A_m/P$. Some key oscillatory parameters of loop oscillations are listed in Table 2.

In order to take a closer look at the oscillating loops in the corona, we arbitrarily extracted the $\mathrm{HRI_{EUV}}$ 174 Å images to show fine-scale coronal loops during the time interval of decayless oscillations, as indicated by two red vertical lines in Figure 3 (a), which happens to cross the oscillating loops 1, 6 and 12. In Figure 3 (b) and (c), we show EUV images at $\mathrm{HRI_{EUV}}$ 174 Å at two fixed instances of time, which contain three oscillating loops, as marked by red curves. The cyan line represents the slit center, which has a constant width of about 675 km (5 pixels), and it is almost perpendicular to the oscillating loop. The green symbol of '$*$' indicates the starting point of the time-distance analysis in panel (a). Based on the $\mathrm{HRI_{EUV}}$ 174 Å images displayed in Figure 3 (b) and (c), the distance between double footpoints of the coronal loop can be estimated. If we assume a semi-circular profile for the coronal loop (cf. Tian et al. 2016; Gao et al. 2022; Li & Chen 2022; Mandal et al. 2022) and consider the projection effect owing to the derived position (e.g., Aschwanden et al. 2002; Kumar et al. 2013; Li 2017), the deprojected loop length (L) could be estimated, as listed in Table 2.

Using the same method (see details in the Appendix A), we manually extracted 6 coronal loop oscillations from slit S2 in region R1 and 10 coronal loop oscillations from slit S3 in region R2, as shown in Figures 4 and 5, respectively. The oscillatory positions of these coronal loop oscillations are manually marked by cyan circles, and they are well fitted by Equation 1, as indicated by magenta curves, implying that they are all decayless oscillations. Some oscillating loops are also shown in the $\mathrm{HRI_{EUV}}$ 174 Å images (see panels (b) and (c) in Figures 4 and 5), which have been outlined by red curves. Then, the loop length can also be estimated by assuming the semi-circular shape (cf. Tian et al. 2016; Gao et al. 2022; Mandal et al. 2022). Coronal loop oscillations with periods longer than 200 s are not considered in this study, for instance, the coronal loop oscillation in the region at around x≈500−1000 s and y≈10 Mm in Figure 5 (a).

At last, a total of 111 coronal loop oscillations are extracted from thirteen slits in the two regions R1 and R2 using the $\mathrm{HRI_{EUV}}$ 174 Å observation. Table 2 lists some key oscillatory parameters based on the fitting results, i.e., the loop length, the oscillatory period, the displacement amplitude, and the velocity amplitude.

3.2. MHD coronal seismology

Assuming that all those decayless oscillations of coronal loops are fundamental mode of standing kink waves, the kink speed (c_k) of transverse oscillations could be determined by the loop length

(L) and the oscillatory period (P), as shown in Equation 2:

$$c_k \approx \frac{2L}{P}, \tag{2}$$

Then, the magnetic field strength (B) inside oscillating loops could be roughly expressed in Equation 3 (e.g., Nakariakov et al. 2003; Nisticò et al. 2013; Li et al. 2017; Anfinogentov & Nakariakov 2019; Gao et al. 2022; Tan 2022; Zhang et al. 2022):

$$B \approx c_k \sqrt{\frac{1+\rho_e/\rho_i}{2}} \sqrt{\mu_0 \widetilde{\mu} \rho_i}\ , \tag{3}$$

Where μ_0 represents the magnetic permittivity of free space, $\mu_0 = 4\pi \times 10^{-7}$ N A^{-2} in the international system of units (SI), and $\widetilde{\mu} \approx 1.27$ stands for an average molecular weight in the solar corona (e.g., Nakariakov & Ofman 2001; Zhang et al. 2020). ρ_e and ρ_i are the external and internal plasma densities of the coronal loop, respectively. In our study, a typical value of the internal plasma density of the coronal loop is applied, such as $\rho_i = 1.67 \times 10^{-12}$ kg m^{-3} ($\sim 10^9$ cm^{-3}), and the density contrast (ρ_e/ρ_i) is assumed to be equal to 1/3 (cf. Gao et al. 2022; Petrova et al. 2022).

Next, we can estimate the wave energy flux of the observed coronal loop oscillations based on the MHD wave seismology (see, Nakariakov & Verwichte 2005; Nakariakov & Kolotkov 2020, for the review articles). Using Equations 4 and 5, the time-averaged wave energy flux (E) carried by the kink-mode MHD wave could be calculated in the oscillating loop (e.g., Goossens et al. 2013; Van Doorsselaere et al. 2014; Yuan & Van Doorsselaere 2016a; Li et al. 2022; Petrova et al. 2022):

$$b \approx A_m \frac{\pi}{L} B, \tag{4}$$

$$E \approx \frac{1}{4} c_k \left(\rho_i\, v_m^2 + \frac{b^2}{\mu_0}\right), \tag{5}$$

where b stands for the Lagrangian perturbation of magnetic fields, namely magnetic field perturbation, which could be estimated by the Lagrangian displacement vector (cf. Yuan & Van Doorsselaere 2016a), A_m and v_m represent the displacement and velocity amplitudes of decayless oscillations, and L, B, c_k, and ρ_i are the loop length, the magnetic field strength, the kink speed, and the plasma density of oscillating loops, respectively. The estimated parameters of decayless oscillations are listed in Table 2. A detailed estimation for the energy flux (E) is given in Appendix B.

4. Statistical results

The observed oscillations in fine-scale coronal loops do not show any systematic decaying, which could be regarded as decayless oscillations. Their main oscillatory parameters are measured,

and the key physical parameters are also estimated based on the MHD coronal seismology, as listed in Table 2. In order to display the distribution of these parameters, we then draw their histograms, as shown in Figures 6 and 7. Next, we will analyze them in details.

4.1. Distribution of key parameters

In total, 111 decayless oscillations are analyzed here, which allowed us to establish the distribution of some key parameters. Figure 6 presents histograms of the loop length (a), the oscillatory period (b), the displacement amplitude (c), and the velocity amplitude (d). Lengths of oscillating loops are measured in the range between about 10.5 Mm and 30.2 Mm, with a median length of 14.4 Mm and an averaged length of 15.1 Mm. They are much shorter than previous measurements of several hundreds Mm in coronal loop oscillations (e.g., Aschwanden et al. 2002; Anfinogentov et al. 2013, 2015; Goddard et al. 2016; Nechaeva et al. 2019), while our estimations are quite similar to those measured in coronal bright points with a length range from 14 Mm to 42 Mm (cf. Gao et al. 2022). Oscillatory periods are in the range of $\sim$11$-$185 s, with a median/averaged period of 40/49 s, which is similar to that detected in decayless oscillations of shorter coronal loops (Petrova et al. 2022), but they are smaller than those in longer coronal loops (Nakariakov et al. 1999; Anfinogentov et al. 2015; Goddard et al. 2016; Mandal et al. 2022). Displacement amplitudes are found to range from roughly 51 km to 488 km, with a median/averaged value of 156/186 km, which is roughly equal to that (170 km on average) in decayless oscillations of coronal loops, but it is larger than those of decayless oscillations in coronal bright points, i.e., ranging from about 27 km to 133 km with an average of 65 km (Gao et al. 2022). Velocity amplitudes are measured in about 5.3$-$118.8 km s^{-1}, with a median/averaged speed of 25.6/29.8 km s^{-1}. Our measurements are similar to those observed in high-frequency decayless waves in coronal loops (Petrova et al. 2022). However, they are much larger than previous findings (several km s^{-1}) obtained in decayless oscillations of loop-like structures (e.g., Tian et al. 2012; Anfinogentov et al. 2013; Nakariakov et al. 2016; Gao et al. 2022; Li et al. 2022).

Figure 7 shows histograms of the kink speed (a), the magnetic field strength (b), the magnetic field perturbation (c), and the energy flux (d). Kink speeds of oscillations loops are $\sim$330$-$1910 km s^{-1} with an averaged speed of 780 km s^{-1}. Magnetic field strengths in oscillating loops are estimated to about 4.1$-$25.2 G with an averaged strength of 9.8 G, which is similar to previous findings using the MHD coronal seismology in coronal loops, i.e., a few Gs to several tens Gs (e.g., Nakariakov & Ofman 2001; Aschwanden et al. 2002; Yang et al. 2020b; Gao et al. 2022; Zhang et al. 2022). Magnetic field perturbations in coronal loops are found to be about 0.07$-$1.5 G with an averaged perturbation of 0.37 G. Finally, energy fluxes taken by decayless oscillations are estimated to range from roughly 7 W m^{-2} to 9220 W m^{-2} with an averaged flux of 820 W m^{-2}, the median flux is only 380 W m^{-2}, implying the lower energy is dominant. The oscillatory and physical parameters estimated from decayless oscillations are summarized in Table 3.

Figure 7 (d) shows that the energy flux carried by decayless oscillations has a broad range, and

they concentrated on the lower energy-end. Hence, we plot the frequency distribution of energy fluxes in log-log space, as shown in Figure 8. It can be seen that the frequency distribution of energy fluxes appears to follow a power-law behavior, which could be expressed by Equation 6:

$$\frac{dN}{dE} = CE^{-\alpha}, \tag{6}$$

where E represents the energy flux carried by decayless oscillations, dN is the number of events in the energy interval [E, E+dE], C and α (power-law index) stands for two constants, which are determined by the maximum likelihood estimation (e.g., Clauset et al. 2009; Verbeeck et al. 2019; Lu et al. 2021). This maximum likelihood method automatically returns a break of the power-low model, as indicated by the vertical line in Figure 8. The dropping of the frequency distribution at higher frequencies is mainly due to the observational fact that a large number of decayless oscillations carried weaker energies are ignored in this study, because we only study these decayless oscillations with periods shorter than 200 s. Therefore, the power-law index is as hard as about 1.12, which is far away from the theoretical expectation, i.e., slightly less than 2.0 (e.g., Hudson 1991; Crosby et al. 1993; Su et al. 2006; Ning et al. 2007; Li et al. 2013, 2016; Ryan et al. 2016).

4.2. Statistical scaling between key parameters

In this subsection, we will establish a statistically significant relationship between several key parameters, as shown in Figure 9. The displacement and velocity amplitudes showed weakly dependence on oscillatory periods or loop lengths (e.g., Nakariakov et al. 2016; Gao et al. 2022), and thus we do not analyze their statistical scaling in this study.

Figure 9 (a) presents the scatter plot between oscillatory periods and loop lengths in norm-norm space. Similar to previous findings (Anfinogentov et al. 2015; Goddard et al. 2016), the oscillatory period linearly (indicated by a magenta line) increases with the length of oscillating loops. Their linear Pearson correlation coefficient (cc.) is as high as 0.98, confirming their strong correlation. Figure 9 (b) shows the scatter plot between oscillatory periods and energy fluxes in log-log space. We find that, despite significant scattering of the two parameters, the energy flux decreases with the growth of the oscillatory period. The negative value of the Pearson correlation coefficient (-0.77) indicates their negative correlation, and the magenta line represents a linear fit.

In Figure 9 (c) we show scatter plots between velocity (black diamonds) and displacement (cyan diamonds) amplitudes and energy fluxes in log-log space. It can be seen that the energy flux linearly (indicated by a magenta line) increases with the speed of velocity amplitudes. However, it is almost not dependent on the displacement amplitude, which shows quite large scattering. The Pearson correlation coefficients confirm that the energy flux is strongly dependent (i.e., 0.97) on the velocity amplitude, but it has weakly dependence (i.e., 0.23) on the displacement amplitude. Figure 9 (d) presents scatter plots between magnetic field perturbations (black squares) or strengths (cyan squares) and energy fluxes in log-log space. From which, we can see that the energy flux

linearly increases with the magnetic field perturbation, as indicated by the magenta line, and their Pearson correlation coefficient is as high as 0.97. Although some scattering, the energy flux appears to increase with the magnetic field strength, and the Pearson correlation coefficient between them is 0.75.

5. Discussions

Thanks to the high-temporal resolution (i.e., ∼3 s) of SoLO/EUI at the passband of HRI_{EUV} 174 Å, 111 short-period decayless oscillations are observed, which have a median period of 40 s. The short-period decayless oscillations have not been detected by SDO/AIA, largely due to their low-temporal resolution, such as 12 s. Due to the small-scale amplitude of decayless oscillations, the motion magnification algorithm is often applied to increase the oscillatory amplitude when using the SDO/AIA data (e.g., Anfinogentov & Nakariakov 2016; Li et al. 2020b; Gao et al. 2022). On the other hand, the small-scale decayless oscillations could be directly detected by SoLO/EUI at the passband of HRI_{EUV} 174 Å, because its high spatial resolution, i.e., 135 km pixel^{-1} in this study. The decayless oscillations are simultaneously detected by SDO/AIA at 171 Å and SoLO/EUI at HRI_{EUV} 174 Å, suggesting that the HRI_{EUV} 174 Å images could be used to study the decayless oscillations (Mandal et al. 2022; Zhong et al. 2022), especially for the decayless oscillations at short periods, i.e., <60 s (Petrova et al. 2022). However, the short-period decayless oscillations correspond to shorter oscillating loops, and these shorter oscillating loops often reveal highly dynamic, such as fast drifting motions, as shown in the animation of eui_174.mp4. Therefore, they could be observed for only persisting over a few wave periods, that is, they can not be seen when the oscillating loop drift away from the slit. In a word, the short-period decayless oscillations are credible (Petrova et al. 2022; Zhong et al. 2022). Next, we will discuss them in details.

5.1. MHD mode of detected decayless oscillations

Transverse oscillations of coronal loops were first discovered in 1999 by TRACE (Aschwanden et al. 1999; Nakariakov et al. 1999), and they raised a great interest in connection with MHD waves and the coronal seismology (e.g., Li et al. 2020; Nakariakov & Kolotkov 2020; Van Doorsselaere et al. 2020; Yang et al. 2020a, b; Nakariakov et al. 2021; Pascoe et al. 2022; Zhong et al. 2022). Transverse loop oscillations have been classified into decaying and decayless oscillations (e.g., Nisticò et al. 2013). In our observations, the decayless oscillations could also be explained by MHD waves. The slow magnetoacoustic wave can be first excluded because it belongs to the longitudinal-mode wave and is often parallel to the oscillating loop (Wang 2011; Yuan et al. 2015; Kolotkov et al. 2019; Nakariakov et al. 2019). Moreover, the local sound speed ($v_s \approx 152\sqrt{\frac{T}{MK}}$) in the coronal loop (cf. Nakariakov & Ofman 2001; Kumar et al. 2013; Li et al. 2017) is estimated to be about 152 km s^{-1}, considering that our observations are taken from the HRI_{EUV} 174 Å channel that has a formation

temperature of about 1 MK. The local sound speed is much slower than the estimated kink speed, as can be seen in Table 3.

Kink speeds are estimated to be 330−1910 km s^{-1}, with an averaged speed of 780 km s^{-1}. The median speed is about 710 km s^{-1}, which is roughly equal to the averaged speed. The estimated kink speeds are much smaller than that requires for the global sausage-mode wave. For this kind of wave, the speed is expected to be in the range of ∼3000−5000 km s^{-1} (e.g. Nakariakov et al. 2003; Inglis et al. 2008). Moreover, the global sausage wave is generally seen in the thicker and denser plasma loop, namely, the density contrast inside and outside the plasma loop should be large enough, i.e., a density contrast of 42 in the flaring loop (cf. Tian et al. 2016). Obviously, the oscillating loops in our study are not satisfied with such high density contrast, although we cannot determine them due to the limited observation. But previous observations have suggested that the typical density contrast of coronal loops are about 2−10 (Aschwanden et al. 2002; Gao et al. 2022; Petrova et al. 2022).

Herein, the measured speeds are very close to the typical kink speed of global kink-mode waves (Nakariakov et al. 2021). The estimated magnetic field strengths are in the range of 4.1−25.2 G, with an average of 9.8 G. Our estimations based on the MHD coronal seismology are quite similar to previous findings derived from the kink oscillation of coronal loops, i.e., several Gs to a few tens Gs (Nakariakov & Ofman 2001; Aschwanden et al. 2002; Long et al. 2017; Zhang et al. 2022). Therefore, the small-scale transverse oscillations observed in coronal loops could be regarded as decayless kink-mode oscillations. Moreover, a strong correlation is found between oscillatory periods and loops lengths (Figure 9 (a)), confirming the explanation of decayless oscillations as the standing kink-mode wave in coronal loops.

5.2. Contribution to the coronal heating

Benefitting from the high-temporal resolution (i.e., ∼3 s) imaging observations observed by SolO/EUI at the HRI_{EUV} 174 Å passband, the averaged period of decayless kink oscillations is estimated to 49 s, while the median period is only 40 s. It is shorter than previous detections in kink oscillations of coronal loops observed by SDO in AIA 171 Å, namely, hundreds of seconds (see, Anfinogentov et al. 2015; Goddard et al. 2016; Nechaeva et al. 2019, for statistical reults). Thus, the decayless kink oscillations are regarded as short-period oscillations (cf. Petrova et al. 2022). Based on the observational fact that oscillatory periods of kink oscillations are always dependent on their loop lengths (Anfinogentov et al. 2015; Goddard et al. 2016; Nechaeva et al. 2019), the short-period kink oscillations should correspond to shorter loops, which is consistent with our measurements (i.e., the averaged loop length is estimated to 15.1 Mm and the median loop length is 14.4 Mm). The measured loop lengths are much shorter than previous findings in coronal loop oscillations with longer periods, which could be as large as several hundreds Mm (e.g., Aschwanden et al. 2002; Anfinogentov et al. 2013).

The averaged displacement amplitude of decayless oscillations is 186 km, with a median value of 156 km. This is quite close to previous findings (170 km on average) in decayless kink oscillations (Anfinogentov et al. 2013, 2015). Obviously, the apparent displacement amplitudes do not gradually decrease with the shorten of oscillatory periods, which agrees with previous findings, for instance, the oscillating amplitude does not reveal any dependence on only one parameter such as oscillatory periods or loop lengths, but it could be determined by both of them (Nakariakov et al. 2016; Gao et al. 2022; Petrova et al. 2022). The displacement amplitudes measured here are mostly equal to the pixel size of HRI_{EUV} 174 Å (135 km) images, which are reasonable. This is because sub-pixel displacement amplitudes have been reported in decayless oscillations in AIA 171 images, and they are demonstrated to be reliable (see, Anfinogentov & Nakariakov 2016; Anfinogentov et al. 2022; Zhong et al. 2021; Gao et al. 2022). The short oscillatory period would lead to a fast velocity amplitude. As being expected, velocity amplitudes of decayless oscillations are found to 5.3−118.8 km s^{-1} with an averaged speed of 29.8 km s^{-1}, which are similar to that of high-frequency decayless waves (Petrova et al. 2022). On the other hand, the velocity amplitude in our study is much larger than previous observations of decayless oscillations observed by SDO/AIA, and it seems to exceed the velocity amplitude of decaying oscillations. Therefore, the previous classification (Nisticò et al. 2013) such as low-amplitude decayless and high-amplitude decaying based on velocity amplitudes is not applicable in this work, and we regarded them as small-scale decayless oscillations.

Kink-mode MHD waves, one of the possible candidates for coronal heating, have been intensively studied since their first detection (see, Van Doorsselaere et al. 2020; Nakariakov et al. 2021, for reviews). Decayless kink oscillations are found to be persistent and omnipresent in solar atmospheres, i.e., coronal loops (Anfinogentov et al. 2013, 2015), prominence threads (Okamoto et al. 2007; Li et al. 2022), coronal bright points with loop-like profiles (Gao et al. 2022). Thus, they could provide continuous energy input that is required to heat the solar corona. However, previous observations found that the dissipating energy carried by decayless kink oscillations were not enough to heat the ambient plasmas in the solar corona (Klimchuk 2015; Li et al. 2022; Gao et al. 2022). On the other hand, a recent high-temporal observation from HRI_{EUV} 174 Å images indicates that the short-period (or high-frequency) decayless kink oscillations take significant energy to supply for heating the quiet corona, even if they only consider the kinetic energy (cf. Petrova et al. 2022).

Given simultaneously consideration of the kinetic and magnetic energies (see, Equation 5), we estimate the energy flux carried by decayless kink oscillations at shorter periods in an active region using the HRI_{EUV} 174 Å images with a time cadence of 3 s. It should be pointed out that we have assumed that the decayless kink oscillations had the same damping mechanism with decaying kink oscillations. And thus, the estimated energy fluxes could also regard as energy losses from decayless kink oscillations, which might be contribution to the coronal heating, as seen in Appendix B. The energy flow in the case of decayless oscillations looks like the following: unknown driver → standing kink oscillations → quick damping → plasma heating. Such process is continuing when the unknown

driver always operates, manifested as 'decayless oscillations'. However, the unknown driver is still an open issue, we will discuss this in Section 5.3. The energy flux is estimated to ∼7−9220 W m^{-2} with an average of 820 W m^{-2}, the median value is as low as 380 W m^{-2}, suggesting that the lower energy is dominant. The minimum energy flux (7 W m^{-2}) taken by the decayless kink oscillation corresponds to a longer oscillatory period (169 s), but the amplitude and the magnetic field are rather low, particularly the velocity amplitude is only 5.3 km s^{-1}, and the magnetic field perturbation is as weak as 0.07 G, as shown in Table 2 (slit S1, loop 12) and Figure 3. The same case of a lower energy flux (40 W m^{-2}) has the longest oscillatory period (185 s) and the weakest magnetic field strength (4.1 G) in this statistic, as seen in Table 2 (slit S2, loop 6) and Figure 4. In contrast, the maximum energy flux (9220 W m^{-2}) carried by the decayless kink oscillation corresponds to a shorter oscillatory period (26 s), while the amplitude and the magnetic field are stronger, particularly the velocity amplitude can reach 118.8 km s^{-1}, and the magnetic field perturbation is as strong as 1.5 G, as seen in Table 2 (slit S1, loop 6) and Figure 3. The same case of a higher energy flux (3970 W m^{-2}) also has the shortest oscillatory period (11 s) and the strongest magnetic field strength (25.2 G) in this statistical study, as seen in Table 2 (slit S3, loop 7) and Figure 5. This is consistent with the scatter plots in Figure 9, which shows that the energy flux is strongly dependent on both the oscillatory period and the magnetic field. However, the maximum energy flux of 9220 W m^{-2} is still not enough to heat the AR corona, such as 10^4 W m^{-2} (cf. Withbroe & Noyes 1977). Moreover, the higher energy flux (i.e., >1000 W m^{-2}) is not dominant (Figure 7), and the energy flux estimated by the expression for the fast kink MHD wave (i.e., Equation 5) is always overestimated (Goossens et al. 2013). In summary, the practical energy carried by the decayless kink MHD wave is not sufficient for heating the AR corona.

5.3. Excitation of decayless kink oscillations

Previous observations suggested that the decaying oscillation could be impulsively excited by an external solar eruption that can be clearly observed, such as solar flares and jets, EUV waves, or flux ropes (e.g., Antolin & Verwichte 2011; Kumar et al. 2013; Reeves et al. 2020; Zhang et al. 2020; Mandal et al. 2022; Zhang et al. 2022). Similarly, the decayless oscillation may be triggered by an impulsive energy release (Nakariakov et al. 2021). On the other hand, the decayless oscillation often lasts for several wave periods or even longer (Tian et al. 2012; Anfinogentov et al. 2015). Hence, the external driver should be continuous to keep the decayless oscillation for a long time, as seen in Appendix B. Now, several theoretical models have been proposed to illustrate the excitation/driver of decayless oscillations, for instance, it might be triggered by the fast magnetoacoustic wave train (Liu et al. 2011; Wang et al. 2012), or it could be excited by the coronal rain caused by a catastrophic cooling process (Verwichte et al. 2017), or it may be a self oscillation that is driven by the slipping interaction between oscillating loops and steady external medium flows (Nakariakov et al. 2016, 2022). However, the triggered eruptions are difficult to detect, largely due to their fine-scale structures, as shown in Figure 10, which presents an overview of our observation.

Figure 10 (a) shows full-disk light curves in the X-rays from 03:05 UT to 04:10 UT on 17 March 2022, which are recorded by SolO/STIX and GOES, respectively. Here, the observed time of GOES has been corrected to the SolO time stamps. There were not solar flares appearing in the HRI_{EUV} observation during 03:18:00−04:02:51 UT, as indicated by the yellow shadow. We note that a small flare erupted at about 03:11 UT, which occurred before the HRI_{EUV} observation. The solar flare is estimated to be a B7 class based on the STIX counts[2]. It was observed by the STIX channels at 4−10 keV and 15−25 keV, but it was impossible to determine the flare location due to the weak counts. Herein, we plot the normalized EUV light curve (normalized to their maximal intensity) integrated over the active region with a FOV of ∼278×278 Mm^2 observed by SDO/AIA at 131 Å, as shown by the cyan line in panel (a). To save the computing time, we use AIA binned (4×4) images with a time cadence of 120 s. Similar to STIX and GOES fluxes, the flare peak also appears in the local EUV flux, indicating that the small flare occurred inside the AR. To identify the flare source, we draw the AIA 131 Å image within a small FOV containing the AR, as shown in Figure 10 (b). The small flare exhibits a bright loop, as marked by the pink arrow. However, we should state that the flare has disappeared before the beginning of decayless oscillation observations. Moreover, most of oscillating loops are far away from the flare source, especially for these oscillating loops in the R1 region. Therefore, the small flare has little impact on the decayless oscillations in our study. Our results are similar to the previous finding, for instance, the solar flare could increase the oscillatory amplitude, but it had little effect on the nature and periods of decayless oscillations (cf. Mandal et al. 2021).

Figure 10 (c) presents the FSI 304 Å image at 03:50:00 UT during our observation. From which, we do not find any coronal mass ejection (CME) or prominence eruptions, implying that the decayless oscillation is impossible to be excited by the precursor of a large-scale solar eruption, i.e., the solar flare, the CME or the erupted prominence. Figure 10 (d) and (e) shows the EUV images with sub-fields (marked by the cyan box in panel (c)) that including the AR measured in wavelengths of $HRI_{Ly\alpha}$ 1216 Å and FSI 304 Å. Similarly, we do not see any small-scale eruptions in these two EUV channels. However, the two EUV images have lower spatial or temporal resolutions, and the observational data is always discontinuous, making it hard to synthesize the animation. Therefore, it is impossible to exclude the possibility that the decayless oscillations are excited by small-scale eruptions, particularly for those small-scale eruptions with short durations, i.e., campfires (Berghmans et al. 2021; Chen et al. 2021), ultraviolet bright points (Li 2022), or fast repeating jets (Chitta et al. 2021; Hou et al. 2021), since they are ubiquitous in the solar corona. On the other hand, the animation of eui_174.mp4 shows that a large number of thread-like structures reveal continuous movements, which might be regarded as steady flows. These steady flows could continuously interact with the oscillating loops, causing decayless oscillations (Nakariakov et al. 2016). In a word, we can conclude that the decayless kink oscillations at short periods could not be excited by large-scale solar eruptions, but they might be triggered by fine-scale solar eruptions, or they could be self oscillations caused by slipping interactions between external flows and oscillating

[2]https://datacenter.stix.i4ds.net/view/plot/lightcurves

loops.

6. Summary

Thanks to the high resolution observation from SolO/EUI at the passband of HRI_{EUV} 174 Å, we present a statistical study of short-period decayless oscillations of coronal loops in the AR NOAA 12965, combining with observations from SolO/FSI, SolO/STIX, SDO/AIA, and GOES, we discuss the excitation of observed decayless kink oscillations, and their contribution to the coronal heating. The main conclusions are summarized as following:

1. A total of 111 oscillating loops are extracted from the AR at the HRI_{EUV} 174 Å passband. They all show transverse oscillations without significant decaying, which could be identified as decayless kink-mode MHD wave of AR coronal loops.

2. A strong correlation is found between oscillatory periods and loop lengths, namely, the oscillatory period increases linearly with the length of oscillating loops, confirming the interpretation of standing kink-mode oscillations of coronal loops.

3. The oscillatory periods of decayless kink oscillations are dominated by shorter periods, i.e., with a median period of 40 s. This is benefitting from the high-temporal ($\sim$3 s) and high-spatial ($\sim$135 km pixel^{-1}) resolution observation measured by SolO/EUI at the channel of HRI_{EUV} 174 Å.

4. The displacement amplitudes of decayless kink oscillations are rather low, but their velocity amplitudes could be as large as 118.8 km s^{-1}. Thus, these decayless kink oscillations could not be called as low-amplitude oscillations, but they are regarded as small-scale oscillations.

5. The energy fluxes carried by decayless kink oscillations are estimated to be 9$-$9220 W m^{-2}, after considering the magnetic energy. They are dominated by energy fluxes below 1000 W m^{-2}, for instance, the averaged energy flux is 820 W m^{-2}, while the median value is only 380 W m^{-2}. So, the decayless kink-mode wave could not be efficiently heating the AR corona, although they might be persistently powered and ongoing dissipating energies that are transferred to the ambient coronal plasmas.

6. The short-period decayless oscillation in the kink mode could be a self-oscillation system excited by the slipping interaction between the external flows and oscillating loops. However, we could not excluded the possibility that it was triggered by a fine-scale solar eruption, mainly due to the lack of higher spatial resolution observations in the chromosphere.

We thank the referee for his/her valuable comments. The author would like to thank the EUI team members for their discussions about the data analysis. This work is funded by the

National Key R&D Program of China 2021YFA1600502 (2021YFA1600500), NSFC under grants 11973092, U1931138, 12073081, 11790302, as well as CAS Strategic Pioneer Program on Space Science, Grant No. XDA15052200, and XDA15320301. D. Li is also supported by the Surface Project of Jiangsu Province (BK20211402). D. M. Long is grateful to the Science Technology and Facilities Council for the award of an Ernest Rutherford Fellowship (ST/R003246/1). Solar Orbiter is a space mission of international collaboration between ESA and NASA, operated by ESA. The EUI instrument was built by CSL, IAS, MPS, MSSL/UCL, PMOD/WRC, ROB, LCF/IO with funding from the Belgian Federal Science Policy Office (BELSPO/PRODEX PEA under contract numbers 4000134088, 4000112292, 4000117262, and 4000134474); the Centre National d'Etudes Spatiales (CNES); the UK Space Agency (UKSA); the Bundesministerium für Wirtschaft und Energie (BMWi) through the Deutsches Zentrum für Luft- und Raumfahrt (DLR); and the Swiss Space Office (SSO). The STIX instrument is an international collaboration between Switzerland, Poland, France, Czech Republic, Germany, Austria, Ireland, and Italy.

REFERENCES

Afanasyev, A. N., Van Doorsselaere, T., & Nakariakov, V. M. 2020, A&A, 633, L8. doi:10.1051/0004-6361/201937187

Anfinogentov, S., Nisticò, G., & Nakariakov, V. M. 2013, A&A, 560, A107. doi:10.1051/0004-6361/201322094

Anfinogentov, S. A., Nakariakov, V. M., & Nisticò, G. 2015, A&A, 583, A136. doi:10.1051/0004-6361/201526195

Anfinogentov, S. & Nakariakov, V. M. 2016, Sol. Phys., 291, 3251. doi:10.1007/s11207-016-1013-z

Anfinogentov, S. A. & Nakariakov, V. M. 2019, ApJ, 884, L40. doi:10.3847/2041-8213/ab4792

Anfinogentov, S. A., Antolin, P., Inglis, A. R., et al. 2022, Space Sci. Rev., 218, 9. doi:10.1007/s11214-021-00869-w

Antolin, P. & Verwichte, E. 2011, ApJ, 736, 121. doi:10.1088/0004-637X/736/2/121

Antolin, P., De Moortel, I., Van Doorsselaere, T., et al. 2016, ApJ, 830, L22. doi:10.3847/2041-8205/830/2/L22

Antolin, P. & Froment, C. 2022, Frontiers in Astronomy and Space Sciences, 9, 820116. doi:10.3389/fspas.2022.820116

Aschwanden, M. J., Fletcher, L., Schrijver, C. J., et al. 1999, ApJ, 520, 880. doi:10.1086/307502

Aschwanden, M. J., de Pontieu, B., Schrijver, C. J., et al. 2002, Sol. Phys., 206, 99. doi:10.1023/A:1014916701283

Aschwanden, M. J. & Boerner, P. 2011, ApJ, 732, 81. doi:10.1088/0004-637X/732/2/81

Berghmans, D., Auchère, F., Long, D. M., et al. 2021, A&A, 656, L4. doi:10.1051/0004-6361/202140380

Chen, S.-X., Li, B., Xia, L.-D., et al. 2015, Sol. Phys., 290, 2231. doi:10.1007/s11207-015-0751-7

Chen, Y., Przybylski, D., Peter, H., et al. 2021, A&A, 656, L7. doi:10.1051/0004-6361/202140638

Chitta, L. P., Solanki, S. K., Peter, H., et al. 2021, A&A, 656, L13. doi:10.1051/0004-6361/202141683

Clauset, A., Shalizi, C. R., & Newman, M. E. J. 2009, SIAM Review, 51, 661. doi:10.1137/070710111

Crosby, N. B., Aschwanden, M. J., & Dennis, B. R. 1993, Sol. Phys., 143, 275. doi:10.1007/BF00646488

De Moortel, I. & Nakariakov, V. M. 2012, Philosophical Transactions of the Royal Society of London Series A, 370, 3193. doi:10.1098/rsta.2011.0640

Díaz, A. J., Oliver, R., Erdélyi, R., et al. 2001, A&A, 379, 1083. doi:10.1051/0004-6361:20011351

Duckenfield, T., Anfinogentov, S. A., Pascoe, D. J., et al. 2018, ApJ, 854, L5. doi:10.3847/2041-8213/aaaaeb

Duckenfield, T. J., Goddard, C. R., Pascoe, D. J., et al. 2019, A&A, 632, A64. doi:10.1051/0004-6361/201936822

Feng, L., Inhester, B., Solanki, S. K., et al. 2007, ApJ, 671, L205. doi:10.1086/525525

Guo, M., Li, B., & Shi, M. 2021, ApJ, 921, L17. doi:10.3847/2041-8213/ac30e3

Gao, Y., Tian, H., Van Doorsselaere, T., et al. 2022, ApJ, 930, 55. doi:10.3847/1538-4357/ac62cf

Goossens, M., Van Doorsselaere, T., Soler, R., et al. 2013, ApJ, 768, 191. doi:10.1088/0004-637X/768/2/191

Goddard, C. R., Nisticò, G., Nakariakov, V. M., et al. 2016, A&A, 585, A137. doi:10.1051/0004-6361/201527341

Goddard, C. R. & Nisticò, G. 2020, A&A, 638, A89. doi:10.1051/0004-6361/202037467

Gupta, G. R., Del Zanna, G., & Mason, H. E. 2019, A&A, 627, A62. doi:10.1051/0004-6361/201935357

Handy, B. N., Acton, L. W., Kankelborg, C. C., et al. 1999, Sol. Phys., 187, 229. doi:10.1023/A:1005166902804

Hindman, B. W. & Jain, R. 2014, ApJ, 784, 103. doi:10.1088/0004-637X/784/2/103

Hou, Z., Tian, H., Berghmans, D., et al. 2021, ApJ, 918, L20. doi:10.3847/2041-8213/ac1f30

Hudson, H. S. 1991, Sol. Phys., 133, 357. doi:10.1007/BF00149894

Inglis, A. R., Nakariakov, V. M., & Melnikov, V. F. 2008, A&A, 487, 1147. doi:10.1051/0004-6361:20079323

Karampelas, K., Van Doorsselaere, T., & Antolin, P. 2017, A&A, 604, A130. doi:10.1051/0004-6361/201730598

Karampelas, K. & Van Doorsselaere, T. 2020, ApJ, 897, L35. doi:10.3847/2041-8213/ab9f38

Klimchuk, J. A. 2015, Philosophical Transactions of the Royal Society of London Series A, 373, 20140256. doi:10.1098/rsta.2014.0256

Kolotkov, D. Y., Nakariakov, V. M., & Zavershinskii, D. I. 2019, A&A, 628, A133. doi:10.1051/0004-6361/201936072

Krucker, S., Hurford, G. J., Grimm, O., et al. 2020, A&A, 642, A15. doi:10.1051/0004-6361/201937362

Kumar, P., Innes, D. E., & Inhester, B. 2013, ApJ, 779, L7. doi:10.1088/2041-8205/779/1/L7

Lemen, J. R., Title, A. M., Akin, D. J., et al. 2012, Sol. Phys., 275, 17. doi:10.1007/s11207-011-9776-8

Li, D., Ning, Z. J., & Wang, J. F. 2013, New A, 23, 19. doi:10.1016/j.newast.2013.02.002

Li, D., Ning, Z. J., Huang, Y., et al. 2017, ApJ, 849, 113. doi:10.3847/1538-4357/aa9073

Li, D. 2017, Research in Astronomy and Astrophysics, 17, 040. doi:10.1088/1674-4527/17/5/40

Li, D., Yuan, D., Su, Y. N., et al. 2018a, A&A, 617, A86. doi:10.1051/0004-6361/201832991

Li, D., Shen, Y., Ning, Z., et al. 2018b, ApJ, 863, 192. doi:10.3847/1538-4357/aad33f

Li, L., Peter, H., Chitta, L. P., et al. 2019, ApJ, 884, 34. doi:10.3847/1538-4357/ab4134

Li, B., Antolin, P., Guo, M.-Z., et al. 2020, Space Sci. Rev., 216, 136. doi:10.1007/s11214-020-00761-z

Li, D., Yuan, D., Goossens, M., et al. 2020a, A&A, 639, A114. doi:10.1051/0004-6361/202038433

Li, D., Li, Y., Lu, L., et al. 2020b, ApJ, 893, L17. doi:10.3847/2041-8213/ab830c

Li, D., Ge, M., Dominique, M., et al. 2021, ApJ, 921, 179. doi:10.3847/1538-4357/ac1c05

Li, D., Xue, J., Yuan, D., et al. 2022, Science China Physics, Mechanics, and Astronomy, 65, 239611. doi:10.1007/s11433-021-1836-y

Li, D. & Chen, W. 2022, ApJ, 931, L28. doi:10.3847/2041-8213/ac6fd2

Li, D. 2022, A&A, 662, A7. doi:10.1051/0004-6361/202142884

Li, Y.-P., Feng, L., Zhang, P., et al. 2016, Research in Astronomy and Astrophysics, 16, 161. doi:10.1088/1674-4527/16/10/161

Liu, W., Title, A. M., Zhao, J., et al. 2011, ApJ, 736, L13. doi:10.1088/2041-8205/736/1/L13

Long, D. M., Valori, G., Pérez-Suárez, D., et al. 2017, A&A, 603, A101. doi:10.1051/0004-6361/201730413

Lopin, I. 2022, MNRAS, 514, 4329. doi:10.1093/mnras/stac1502

Lu, L., Feng, L., Li, D., et al. 2021, ApJS, 253, 29. doi:10.3847/1538-4365/abd79b

Mac Cormack, C., López Fuentes, M., Mandrini, C. H., et al. 2022, arXiv:2206.09921

Mandal, S., Tian, H., & Peter, H. 2021, A&A, 652, L3. doi:10.1051/0004-6361/202141542

Mandal, S., Chitta, L. P., Antolin, P., et al. 2022, A&A, 666, L2. doi:10.1051/0004-6361/202244403

Mariska, J. T. & Muglach, K. 2010, ApJ, 713, 573. doi:10.1088/0004-637X/713/1/573

Mierla, M., Zhukov, A. N., Berghmans, D., et al. 2022, A&A, 662, L5. doi:10.1051/0004-6361/202244020

Morton, R. J., Verth, G., Jess, D. B., et al. 2012, Nature Communications, 3, 1315. doi:10.1038/ncomms2324

Müller, D., St. Cyr, O. C., Zouganelis, I., et al. 2020, A&A, 642, A1. doi:10.1051/0004-6361/202038467

Nakariakov, V. M., Ofman, L., Deluca, E. E., et al. 1999, Science, 285, 862. doi:10.1126/science.285.5429.862

Nakariakov, V. M. & Ofman, L. 2001, A&A, 372, L53. doi:10.1051/0004-6361:20010607

Nakariakov, V. M., Melnikov, V. F., & Reznikova, V. E. 2003, A&A, 412, L7. doi:10.1051/0004-6361:20031660

Nakariakov, V. M. & Verwichte, E. 2005, Living Reviews in Solar Physics, 2, 3. doi:10.12942/lrsp-2005-3

Nakariakov, V. M., Anfinogentov, S. A., Nisticò, G., et al. 2016, A&A, 591, L5. doi:10.1051/0004-6361/201628850

Nakariakov, V. M., Kosak, M. K., Kolotkov, D. Y., et al. 2019, ApJ, 874, L1. doi:10.3847/2041-8213/ab0c9f

Nakariakov, V. M. & Kolotkov, D. Y. 2020, ARA&A, 58, 441. doi:10.1146/annurev-astro-032320-042940

Nakariakov, V. M., Anfinogentov, S. A., Antolin, P., et al. 2021, Space Sci. Rev., 217, 73. doi:10.1007/s11214-021-00847-2

Nakariakov, V. M., Kolotkov, D. Y., & Zhong, S. 2022, MNRAS, 516, 5227. doi:10.1093/mnras/stac2628

Nechaeva, A., Zimovets, I. V., Nakariakov, V. M., et al. 2019, ApJS, 241, 31. doi:10.3847/1538-4365/ab0e86

Ning, Z., Wu, H., Xu, F., et al. 2007, Sol. Phys., 242, 101. doi:10.1007/s11207-007-0412-6

Ning, Z., Cao, W., Okamoto, T. J., et al. 2009, A&A, 499, 595. doi:10.1051/0004-6361/200810853

Ning, Z., Wang, Y., Hong, Z., et al. 2022, Sol. Phys., 297, 2. doi:10.1007/s11207-021-01935-w

Nisticò, G., Nakariakov, V. M., & Verwichte, E. 2013, A&A, 552, A57. doi:10.1051/0004-6361/201220676

Ofman, L. & Wang, T. 2002, ApJ, 580, L85. doi:10.1086/345548

Okamoto, T. J., Tsuneta, S., Berger, T. E., et al. 2007, Science, 318, 1577. doi:10.1126/science.1145447

Pascoe, D. J., Van Doorsselaere, T., & De Moortel, I. 2022, ApJ, 929, 101. doi:10.3847/1538-4357/ac5e30

Pesnell, W. D., Thompson, B. J., & Chamberlin, P. C. 2012, Sol. Phys., 275, 3. doi:10.1007/s11207-011-9841-3

Peter, H., Bingert, S., Klimchuk, J. A., et al. 2013, A&A, 556, A104. doi:10.1051/0004-6361/201321826

Peter, H. & Bingert, S. 2012, A&A, 548, A1. doi:10.1051/0004-6361/201219473

Petrova, E., Magyar, N., Van Doorsselaere, T., et al. 2022, arXiv:2205.05319

Reale, F. 2014, Living Reviews in Solar Physics, 11, 4. doi:10.12942/lrsp-2014-4

Reeves, K. K., Polito, V., Chen, B., et al. 2020, ApJ, 905, 165. doi:10.3847/1538-4357/abc4e0

Rochus, P., Auchère, F., Berghmans, D., et al. 2020, A&A, 642, A8. doi:10.1051/0004-6361/201936663

Ruderman, M. S. & Petrukhin, N. S. 2021, MNRAS, 501, 3017. doi:10.1093/mnras/staa3816

Ryan, D. F., Dominique, M., Seaton, D., et al. 2016, A&A, 592, A133. doi:10.1051/0004-6361/201628130

Sadeghi, M. & Karami, K. 2019, ApJ, 879, 121. doi:10.3847/1538-4357/ab24c4

Shen, Y., Liu, Y., Tian, Z., et al. 2017, ApJ, 851, 101. doi:10.3847/1538-4357/aa9af0

Shen, Y., Tang, Z., Miao, Y., et al. 2018a, ApJ, 860, L8. doi:10.3847/2041-8213/aac8dd

Shen, Y., Tang, Z., Li, H., et al. 2018, MNRAS, 480, L63. doi:10.1093/mnrasl/sly127

Shi, M., Van Doorsselaere, T., Guo, M., et al. 2021, ApJ, 908, 233. doi:10.3847/1538-4357/abda54

Su, Y., Gan, W. Q., & Li, Y. P. 2006, Sol. Phys., 238, 61. doi:10.1007/s11207-006-0156-8

Su, W., Guo, Y., Erdélyi, R., et al. 2018, Scientific Reports, 8, 4471. doi:10.1038/s41598-018-22796-7

Tan, B. 2022, Research in Astronomy and Astrophysics, 22, 072001. doi:10.1088/1674-4527/ac6f4b

Tian, H., McIntosh, S. W., Wang, T., et al. 2012, ApJ, 759, 144. doi:10.1088/0004-637X/759/2/144

Tian, H., DeLuca, E. E., Cranmer, S. R., et al. 2014, Science, 346, 1255711. doi:10.1126/science.1255711

Tian, H., Young, P. R., Reeves, K. K., et al. 2016, ApJ, 823, L16. doi:10.3847/2041-8205/823/1/L16

Van Doorsselaere, T., De Groof, A., Zender, J., et al. 2011, ApJ, 740, 90. doi:10.1088/0004-637X/740/2/90

Van Doorsselaere, T., Gijsen, S. E., Andries, J., et al. 2014, ApJ, 795, 18. doi:10.1088/0004-637X/795/1/18

Van Doorsselaere, T., Srivastava, A. K., Antolin, P., et al. 2020, Space Sci. Rev., 216, 140. doi:10.1007/s11214-020-00770-y

Verbeeck, C., Kraaikamp, E., Ryan, D. F., et al. 2019, ApJ, 884, 50. doi:10.3847/1538-4357/ab3425

Verwichte, E., Antolin, P., Rowlands, G., et al. 2017, A&A, 598, A57. doi:10.1051/0004-6361/201629634

Wang, T. 2011, Space Sci. Rev., 158, 397. doi:10.1007/s11214-010-9716-1

Wang, T., Ofman, L., Davila, J. M., et al. 2012, ApJ, 751, L27. doi:10.1088/2041-8205/751/2/L27

Wang, T., Ofman, L., Yuan, D., et al. 2021, Space Sci. Rev., 217, 34. doi:10.1007/s11214-021-00811-0

Watko, J. A. & Klimchuk, J. A. 2000, Sol. Phys., 193, 77. doi:10.1023/A:1005209528612

Withbroe, G. L. & Noyes, R. W. 1977, ARA&A, 15, 363. doi:10.1146/annurev.aa.15.090177.002051

Williams, T., Walsh, R. W., & Morgan, H. 2021, ApJ, 919, 47. doi:10.3847/1538-4357/ac0f76

Yang, Z., Tian, H., Tomczyk, S., et al. 2020a, Science in China E: Technological Sciences, 63, 2357. doi:10.1007/s11431-020-1706-9

Yang, Z., Bethge, C., Tian, H., et al. 2020b, Science, 369, 694. doi:10.1126/science.abb4462

Yuan, D., Van Doorsselaere, T., Banerjee, D., et al. 2015, ApJ, 807, 98. doi:10.1088/0004-637X/807/1/98

Yuan, D. & Van Doorsselaere, T. 2016a, ApJS, 223, 23. doi:10.3847/0067-0049/223/2/23

Yuan, D. & Van Doorsselaere, T. 2016b, ApJS, 223, 24. doi:10.3847/0067-0049/223/2/24

Yuan, D., Li, B., & Walsh, R. W. 2016, ApJ, 828, 17. doi:10.3847/0004-637X/828/1/17

Zhang, Q. M., Dai, J., Xu, Z., et al. 2020, A&A, 638, A32. doi:10.1051/0004-6361/202038233

Zhang, Q. M. 2020, A&A, 642, A159. doi:10.1051/0004-6361/202038557

Zhang, Q. M., Chen, J. L., Li, S. T., et al. 2022, Sol. Phys., 297, 18. doi:10.1007/s11207-022-01952-3

Zhong, S., Duckenfield, T. J., Nakariakov, V. M., et al. 2021, Sol. Phys., 296, 135. doi:10.1007/s11207-021-01870-w

Zhong, S., Nakariakov, V. M., Kolotkov, D. Y., et al. 2022, MNRAS, 516, 5989. doi:10.1093/mnras/stac2545

Zhou, G. P., Zhang, J., & Wang, J. X. 2016, ApJ, 823, L19. doi:10.3847/2041-8205/823/1/L19

Zimovets, I. V. & Nakariakov, V. M. 2015, A&A, 577, A4. doi:10.1051/0004-6361/201424960

Table 1: Observed Instruments used in this study.

Telescope	Wavelength	Time cadence (s)	Pixel scale (km)	Channel	Time (UT)
SolO/EUI	174 Å	∼3	∼135	EUV	03:18:00−04:02:51
	1216 Å	∼5	∼282	Lyα	03:18:00−03:46:55
SolO/FSI	304 Å	∼60	∼1219	EUV	03:50:00−04:03:00
SDO/AIA	171 Å	12	∼435	EUV	–
	131 Å	120	∼1740	EUV	–
	4−10 keV	∼4	–	SXR	
SolO/STIX	10−15 keV	∼4	–	SXR	02:49:49−06:09:57
	15−25 keV	∼4	–	SXR/HXR	
GOES	1−8 Å	∼1	–	SXR	–

Table 2:: Key parameters measured in oscillating loops.

Slit	Loops	L (Mm)	P (s)	A_m (km)	v_m (km s^{-1})	c_k (km s^{-1})	B (G)	b (G)	E (W m^{-2})
	1	18.4	76	275	22.6	480	6.0	0.28	180
	2	14.9	56	181	20.2	530	6.6	0.25	160
	3	11.2	25	156	39.0	890	11.2	0.49	990
	4	10.9	24	386	97.5	880	11.0	1.22	6100
	5	10.7	22	126	35.5	960	12.1	0.45	880
	6	11.5	26	488	118.8	890	11.2	1.50	9220
	7	24.9	145	148	6.4	340	4.3	0.08	10
S1	8	16.4	62	259	26.2	530	6.6	0.33	270
	9	11.7	26	164	39.5	900	11.3	0.50	1020
	10	13.5	34	177	33.2	800	10.1	0.42	650
	11	12.4	33	249	47.1	750	9.4	0.59	1210
	12	29.2	169	144	5.3	350	4.3	0.07	7
	13	22.9	113	421	23.4	410	5.1	0.29	160
	1	12.8	25	98	24.7	1020	12.9	0.31	460
	2	15.7	47	254	33.6	660	8.3	0.42	550
S2	3	17.1	70	350	31.5	490	6.1	0.40	350
	4	12.3	26	152	36.8	950	11.9	0.46	940
	5	11.8	20	164	52.4	1200	15.1	0.66	2410
	6	30.2	185	358	12.1	330	4.1	0.15	40
	1	11.2	26	132	32.0	860	10.8	0.40	650
	2	22.3	113	352	19.6	390	4.9	0.25	110
	3	13.3	32	124	24.7	840	10.6	0.31	380
	4	16.4	62	147	14.9	530	6.7	0.19	90
S3	5	16.5	62	131	13.2	530	6.7	0.17	70

	6	14.9	40	255	39.6	740	9.3	0.50	850
	7	10.5	11	91	52.0	1910	25.2	0.69	3970
	8	15.4	44	52	7.4	700	8.8	0.09	30
	9	15.9	54	122	14.2	590	7.4	0.18	90
	10	15.8	53	263	31.2	600	7.5	0.39	430
	1	11.9	25	168	41.5	940	11.8	0.52	1180
	2	16.0	49	439	56.2	650	8.2	0.71	1510
	3	21.9	115	148	8.1	380	4.8	0.10	20
S4	4	16.1	49	118	15.1	650	8.2	0.19	110
	5	13.3	37	140	23.8	720	9.0	0.30	300
	6	14.5	45	237	33.2	640	8.1	0.42	520
	1	13.8	30	185	39.0	930	11.7	0.49	1030
	2	11.9	24	201	53.0	1000	12.5	0.67	2050
	3	15.7	50	239	30.1	630	7.9	0.38	420
S5	4	13.7	30	157	33.4	920	11.6	0.42	750
	5	10.8	21	186	55.1	1020	12.8	0.69	2260
	6	14.0	36	189	33.5	790	9.9	0.42	640
	7	12.0	26	141	33.4	900	11.4	0.42	740
	1	22.9	120	367	19.2	380	4.8	0.24	100
	2	16.8	66	180	17.1	510	6.4	0.21	110
S6	3	12.5	27	343	81.0	940	11.8	1.0	4500
	4	16.6	54	138	16.0	610	7.7	0.20	120
	5	16.7	57	153	16.9	590	7.4	0.21	120
	1	13.5	37	200	33.5	720	9.0	0.42	590
	2	15.3	49	219	28.0	630	7.9	0.35	360
	3	21.2	98	126	8.1	430	5.4	0.10	20
S7	4	15.1	44	176	25.2	690	8.7	0.32	320
	5	10.5	23	83	22.7	910	11.5	0.29	350
	6	15.2	54	334	39.1	570	7.1	0.49	640
	7	14.9	53	164	19.2	560	7.0	0.24	150
	8	24.6	135	385	18.0	360	4.6	0.23	90
	1	18.8	77	324	26.5	490	6.2	0.33	250
	2	13.9	39	433	69.7	710	8.9	0.88	2520
S8	3	13.6	38	280	46.1	720	9.0	0.58	1110
	4	13.9	40	211	32.8	690	8.7	0.41	510
	5	14.1	40	201	31.6	710	8.9	0.40	510
	6	16.5	58	326	35.4	570	7.2	0.44	520
	1	14.4	42	139	20.9	690	8.6	0.26	220
	2	13.2	27	129	30.5	990	12.4	0.38	670
	3	12.4	17	98	36.6	1480	18.5	0.46	1450

	4	13.0	23	77	20.9	1130	14.2	0.26	360
	5	13.0	23	152	41.2	1130	14.2	0.52	1400
	6	14.0	38	157	25.7	730	9.2	0.32	350
	7	12.5	17	131	48.0	1450	18.2	0.60	2440
	8	13.6	26	162	39.3	1050	13.1	0.49	1180
S9	9	12.8	23	104	28.3	1110	13.9	0.36	650
	10	14.2	37	201	33.9	760	9.6	0.43	640
	11	18.2	73	450	38.8	500	6.3	0.49	550
	12	13.1	25	151	38.6	1070	13.4	0.48	1160
	13	14.8	39	115	18.5	760	9.5	0.23	190
	14	15.5	49	132	17.0	630	8.0	0.21	130
	15	14.6	41	92	14.0	710	8.9	0.18	100
	16	13.2	26	174	42.7	1030	12.9	0.54	1370
	17	21.8	113	119	6.6	390	4.9	0.08	10
	18	14.4	41	293	45.5	710	8.9	0.57	1080
	1	13.6	30	84	17.8	920	11.5	0.22	210
	2	11.0	13	133	63.1	1670	21.0	0.79	4870
	3	14.5	44	143	20.6	670	8.4	0.26	210
	4	13.8	32	221	43.1	860	10.8	0.54	1160
	5	13.3	29	398	86.4	920	11.5	1.09	5020
	6	15.7	50	175	22.2	640	8.0	0.28	230
S10	7	16.1	53	102	12.2	610	7.6	0.15	70
	8	15.2	47	123	16.2	640	8.1	0.20	120
	9	16.4	55	108	12.3	590	7.4	0.15	70
	10	17.1	62	87	8.8	550	6.9	0.11	30
	11	12.7	22	88	25.6	1170	14.7	0.32	560
	12	12.0	17	68	25.5	1430	18.1	0.32	680
	13	12.8	21	90	26.9	1220	15.4	0.34	640
	14	10.9	15	51	21.7	1490	18.7	0.27	520
	15	11.5	18	73	25.7	1290	16.2	0.32	620
	1	17.1	66	208	19.9	520	6.5	0.25	150
	2	16.0	53	169	20.1	610	7.6	0.25	180
S11	3	15.3	48	174	23.0	640	8.1	0.29	250
	4	14.5	43	112	16.6	680	8.6	0.21	140
	1	22.0	112	305	17.1	400	4.9	0.22	80
	2	12.6	22	71	20.2	1150	14.5	0.25	350
S12	3	12.5	22	70	20.3	1150	14.4	0.26	350
	4	12.8	23	73	20.3	1130	14.2	0.25	340
	5	15.5	49	74	9.5	640	8.0	0.12	40
	6	15.8	50	111	14.0	630	7.9	0.18	90

	1	16.3	62	149	15.1	530	6.6	0.19	90
	2	10.9	20	80	25.6	1120	14.0	0.32	530
	3	15.6	58	170	18.4	540	6.8	0.23	130
S13	4	16.0	60	132	13.8	530	6.7	0.17	70
	5	11.3	23	123	34.2	990	12.5	0.43	850
	6	11.2	23	146	40.6	990	12.5	0.51	1200
	7	27.1	165	249	9.5	330	4.1	0.12	20

Table 3: Statistical results of key parameters measured in 111 oscillating loops.

	Minimum	Maximum	Median	Average	Standard deviation
L (Mm)	10.5	30.2	14.4	15.1	3.8
P (s)	11	185	40	49	34
A_m (km)	51	488	156	186	99
v_m (km s^{-1})	5.3	118.8	25.6	29.8	18.5
c_k (km s^{-1})	330	1910	710	780	300
B (G)	4.1	25.2	8.9	9.8	3.8
b (G)	0.07	1.5	0.32	0.37	0.23
E (W m^{-2})	7	9220	380	820	1340

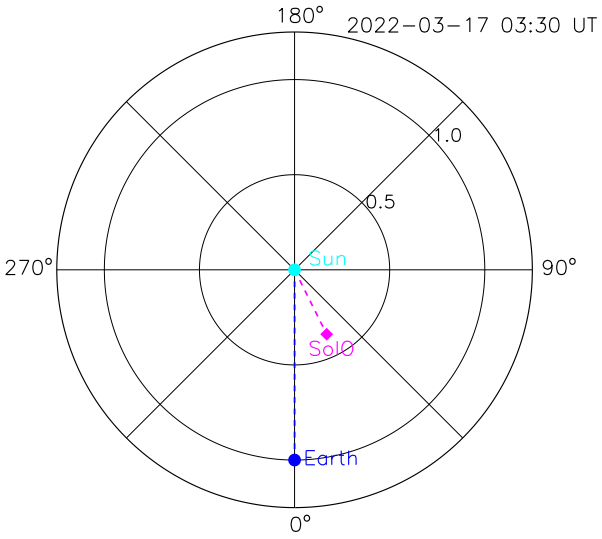

Fig. 1.— Sketch plot of the location of SolO with respect to the Earth at 03:30 UT on 17 March 2022, in Heliocentric-Earth equatorial coordinates.

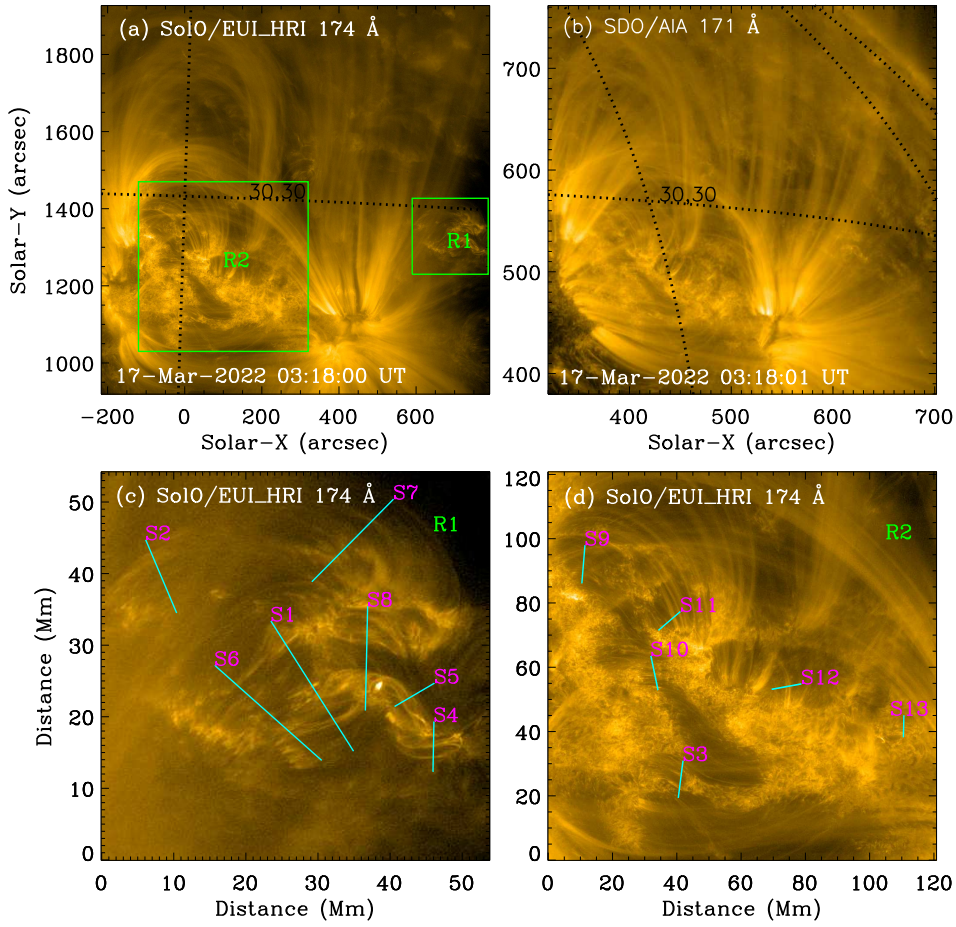

Fig. 2.— Upper: Overview of coronal loops on 17 March 2022 as seen by SolO/EUI at HRI_{EUV} 174 Å (a), and SDO/AIA 171 Å (b). The dotted lines mark the latitude-longitude grids. Bottom: Sub-fields corresponding to two green boxes (R1 and R2) marked in panel (a). The cyan lines outline thirteen slits that are crossed to coronal loops. An animation provided in the online version shows the temporal evolution of coronal loops in two zoomed images (R1 and R2) at HRI_{EUV} 174 Å.

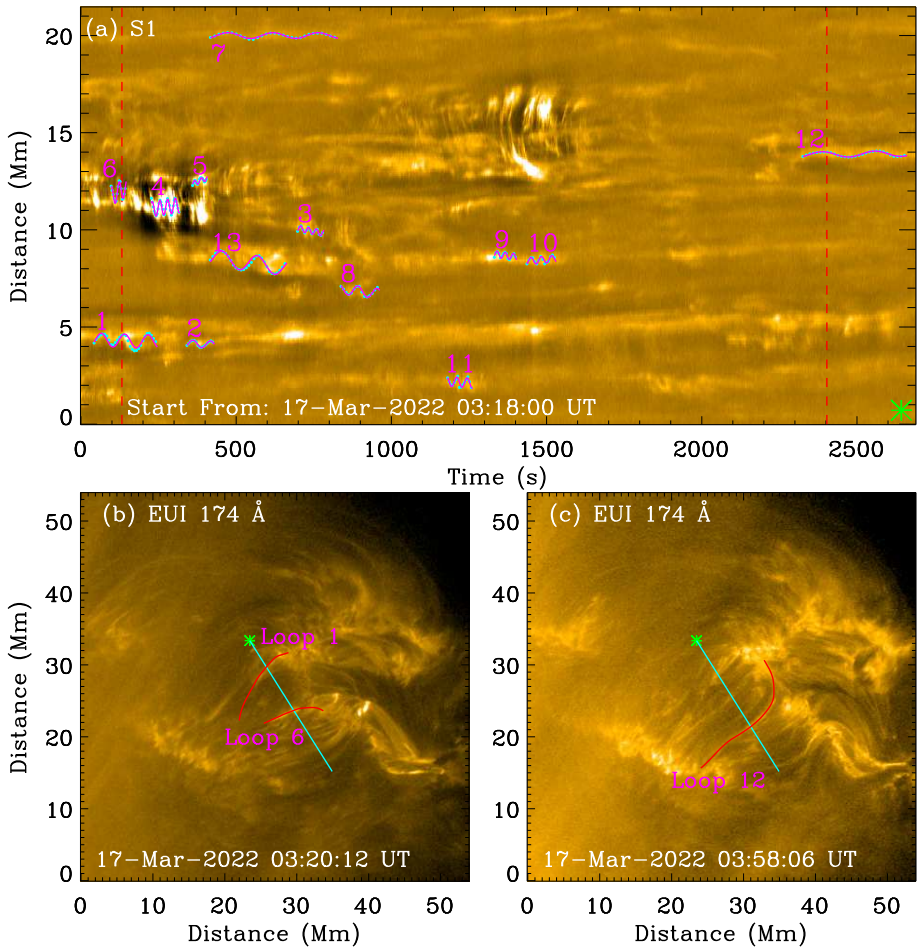

Fig. 3.— Panel (a): The time-distance map made from slit S1 in region R1. The cyan circles indicate the fitting profile positions of coronal loop oscillations, and the magenta curves represent their best fitting results. Two vertical dashed lines outline the time in panels (b) & (c), respectively. Panels (b) & (c): Two EUV images show the interested coronal loops (1, 6 and 12), as marked by the red curves. The cyan line indicates the slit position, and the green symbol ('∗') denotes the starting point of the time-distance analysis.

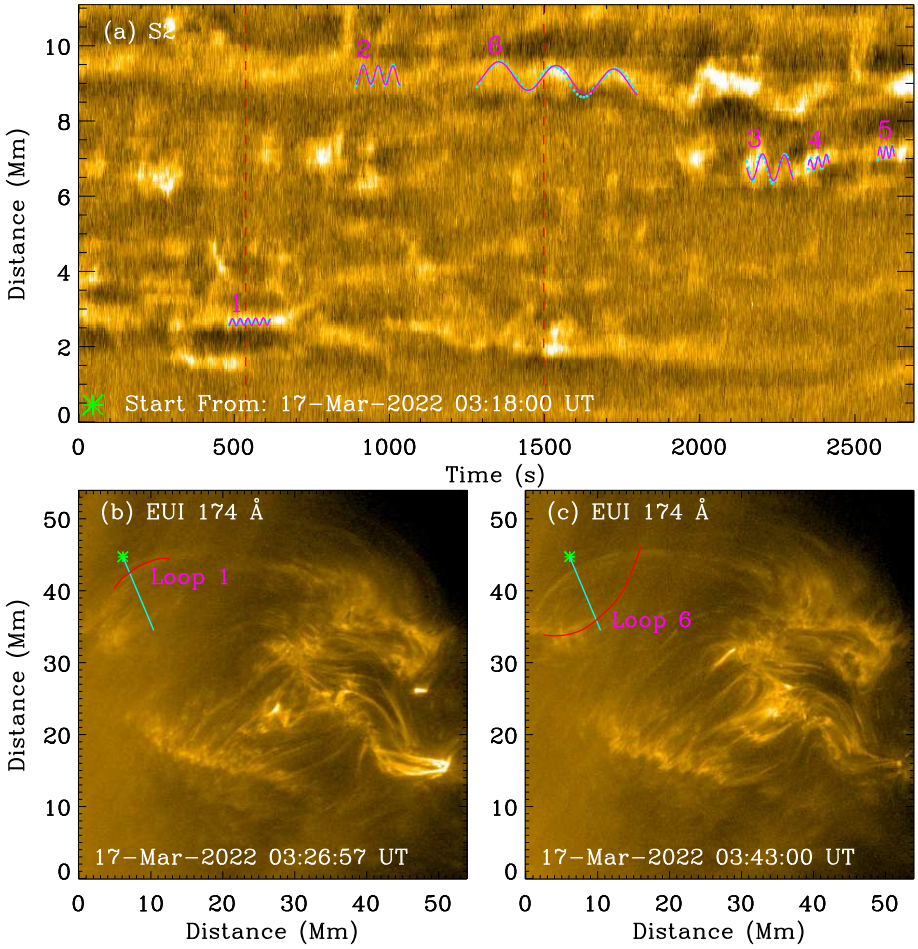

Fig. 4.— Similar to Figure 3 but the analysis is made for slit S2 in region R1.

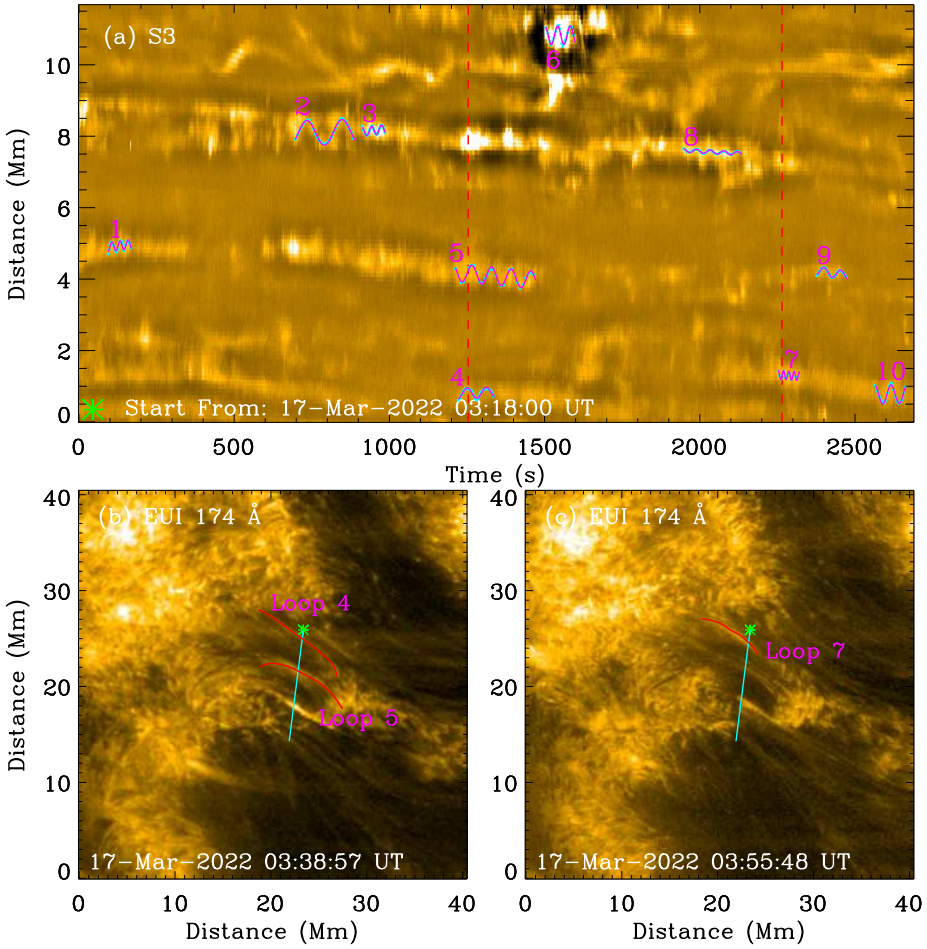

Fig. 5.— Similar to Figure 3 but the analysis is made for slit S3 in region R2.

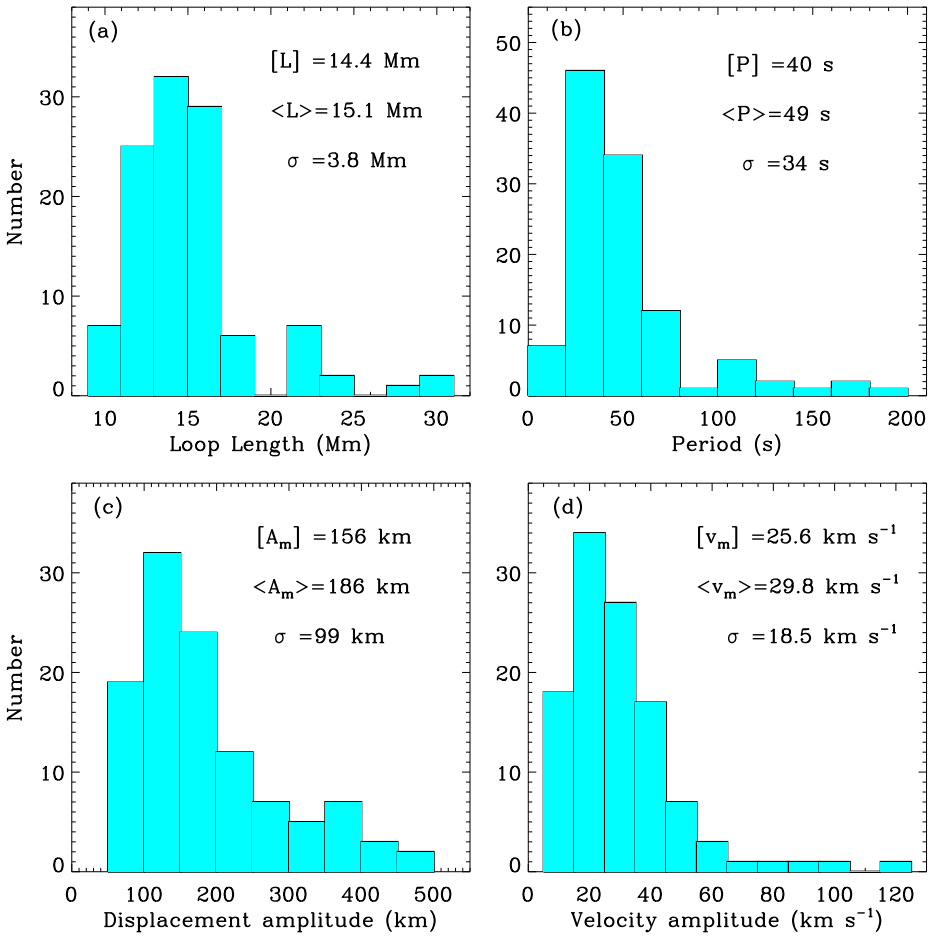

Fig. 6.— Distributions of the main oscillatory parameters: loop length (a), oscillatory period (b), displacement amplitude (c), and velocity amplitude (d). The median ([ ]) values, average (<>) values and standard deviations (σ) for the corresponding parameters are labeled in each panel.

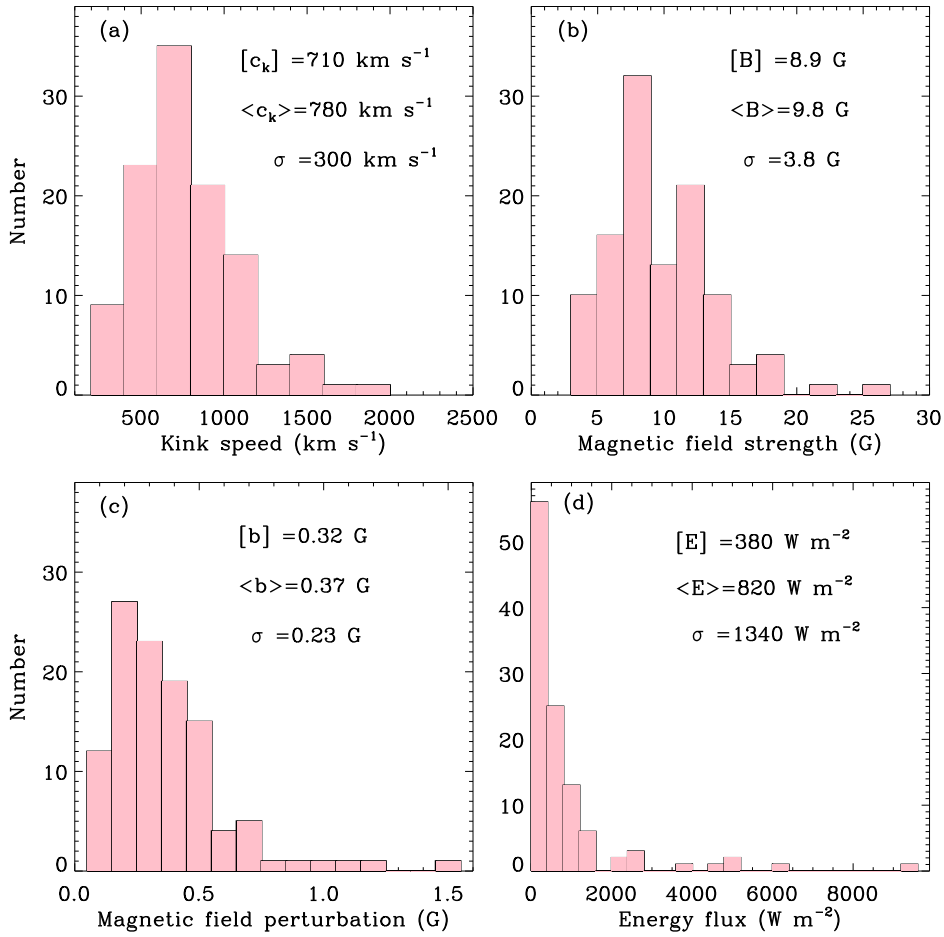

Fig. 7.— Distributions of the key physical parameters from coronal loop oscillations: kink speed (a), magnetic field strength (b), magnetic field perturbation (c), and energy flux (d). The median ([ ]) values, average (<>) values and standard deviations (σ) for the corresponding parameters are labeled in each panel.

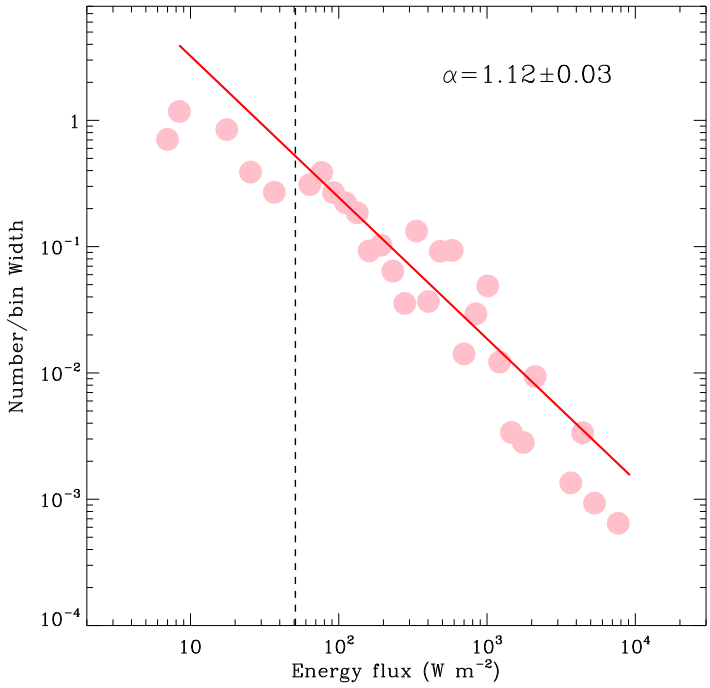

Fig. 8.— The frequency distribution as a function of the energy flux in log-log space. The power-law index (α) is estimated by the maximum likelihood method. The vertical line indicates the low energy cutoff, and the red line represents the power-law model.

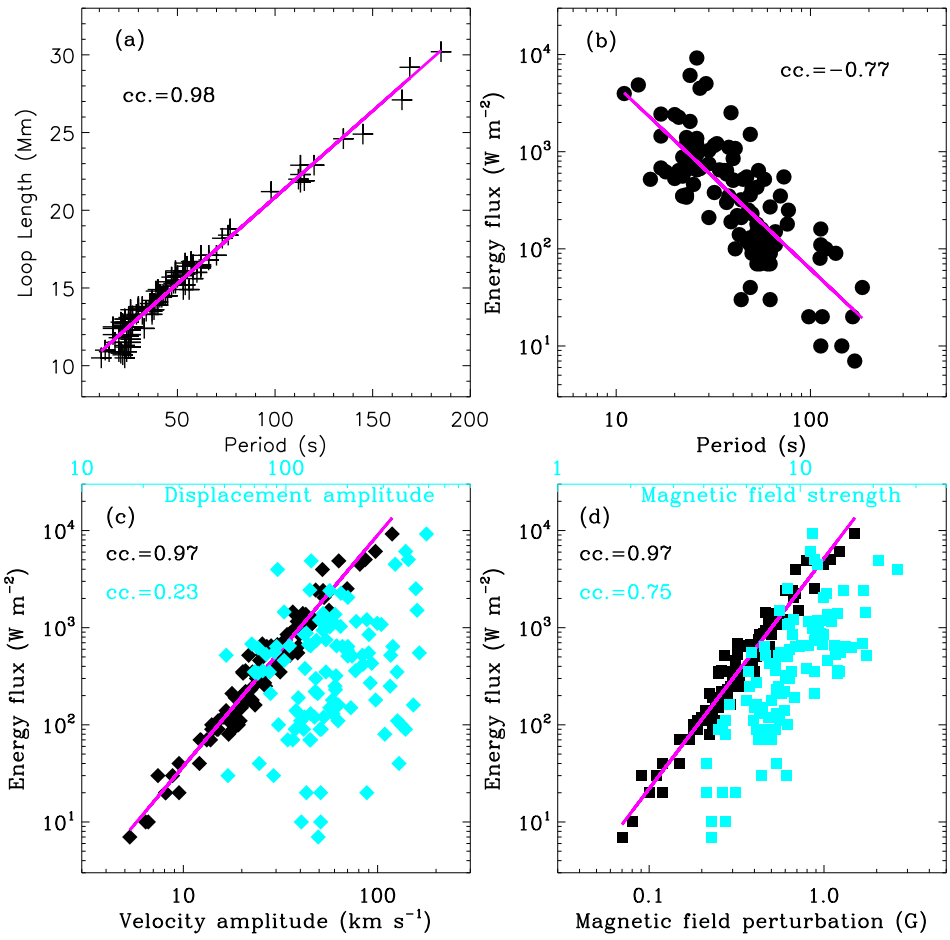

Fig. 9.— Scatter plots between two key parameters of coronal loop oscillations: oscillatory periods vs. loop lengths (a), oscillatory periods vs. energy flux (b), velocity amplitudes (black) and displacement amplitude (cyan) vs. energy flux (c), magnetic field perturbation (black) and magnetic field strength (cyan) vs. energy flux (d). The Pearson correlation coefficients (cc.) are also provided. The magenta line indicates a linear fit in each panel.

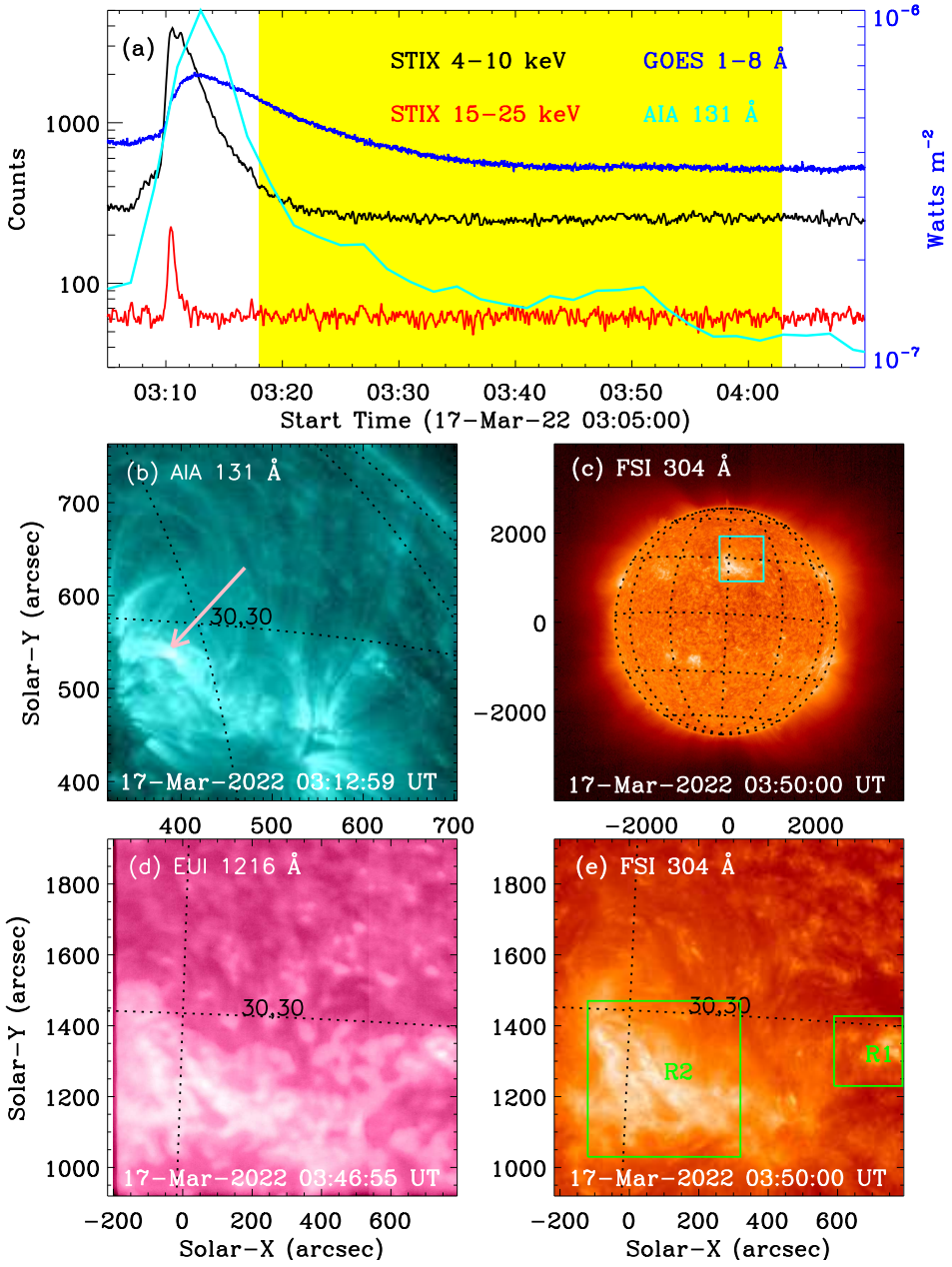

Fig. 10.— Panel (a): Multi-wavelength time series during 03:05−04:10 UT on 17 March 2022, namely full-disk light curves recorded by GOES 1−8 Å(blue), STIX 4−10 keV (black), 10−15 keV (red) and 15−25 keV (green), and the local flux integrated over the active region in AIA 131 Å as normalization by the maximal intensity. The yellow shadow indicates the observational duration of SolO/EUI 174 Å. Panel (b): SDO/AIA 131 Å image shows the active region used to integrate the local flux, the pink arrow indicates the flare site. Panel (c): SolO/FSI 304 map shows the full Sun, the cyan box outlines the interested active region. The dotted lines mark the latitude-longitude grids. Panels (d) and (e): EUV images show the interested active region (cyan box in panel (c)), observed by SolO/EUI at Lyα 1216 Å, and SolO/FSI at 304 Å, respectively. The green boxes outline the same sub-fields in Figure 2

A. Zoomed time-distance images

Figures 3–5 present time-distance maps along longer slits during the whole observational time, i.e., from 03:18:00 UT to 04:02:51 UT. Thus, some decayless oscillations could be not very obvious, mainly due to their small-scale amplitudes overplotted on the large FOV map. Actually, the small-scale oscillation with a short period is identified from the zoomed time-distance map one by one, as shown in Figures A1–A3. Figure A1 displays two zoomed time-distance maps along slit 1 in region R1, corresponding to the oscillating loops 1 (a) and 12 (b), respectively. Those cyan circles mark the central positions of the oscillating loops. Similar to previous studies (Anfinogentov et al. 2013, 2015), the loop centers are not determined by Gaussian fitting. This is because that another coronal loop without any oscillatory signature is overlapping on the oscillating loop, as indicated by two pink arrows. On the other hand, the loop centers of some oscillating loops are difficult to identify, due to the overlap of multiple loops. In such case, the loop edges are used to study their oscillations according to the assumption of constant cross-sectional loops (cf. Williams et al. 2021; Gao et al. 2022), as shown in Figure A2 (b) and Figure A3 (a).

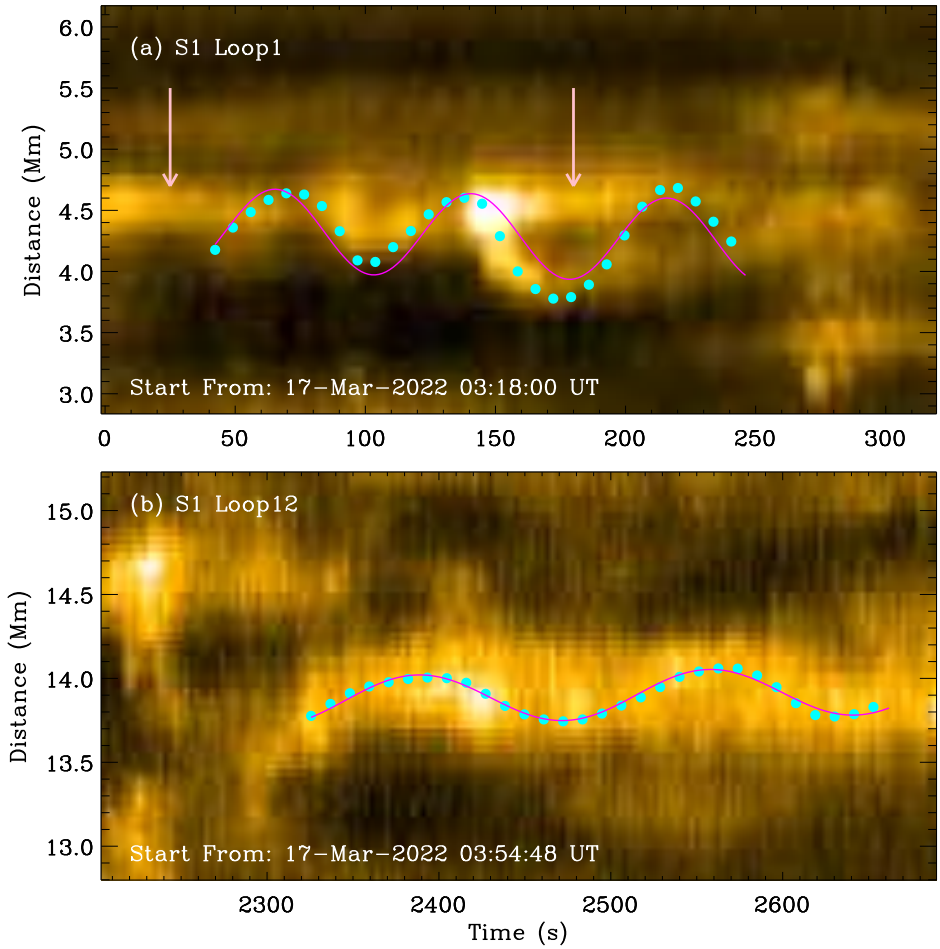

Fig. A1.— Zoomed time-distance maps made from slit S1 in region R1 along the oscillating loops 1 (a) and 12 (b). The cyan circles indicate the fitting profile positions of coronal loop oscillations, and the magenta curves represent their best fitting results.

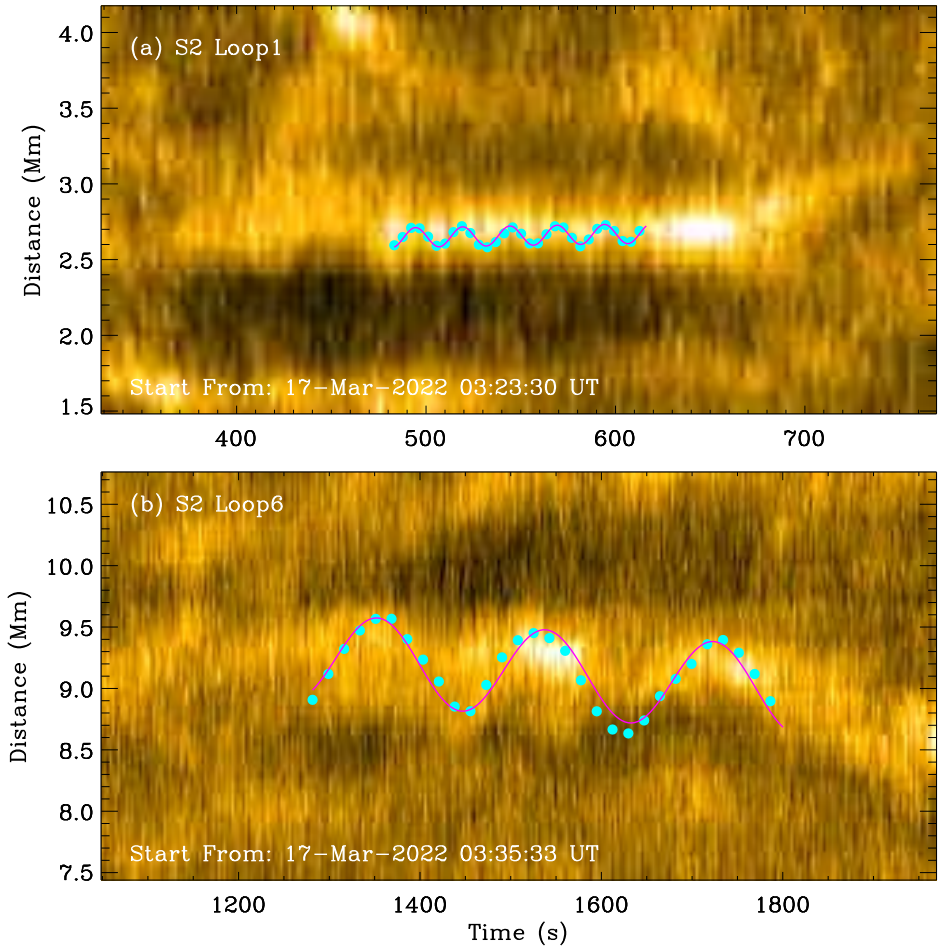

Fig. A2.— Zoomed time-distance diagrams made from slit S2 in region R1 along the oscillating loops 1 (a) and 6 (b). The cyan circles indicate the fitting profile positions of coronal loop oscillations, and the magenta curves represent their best fitting results.

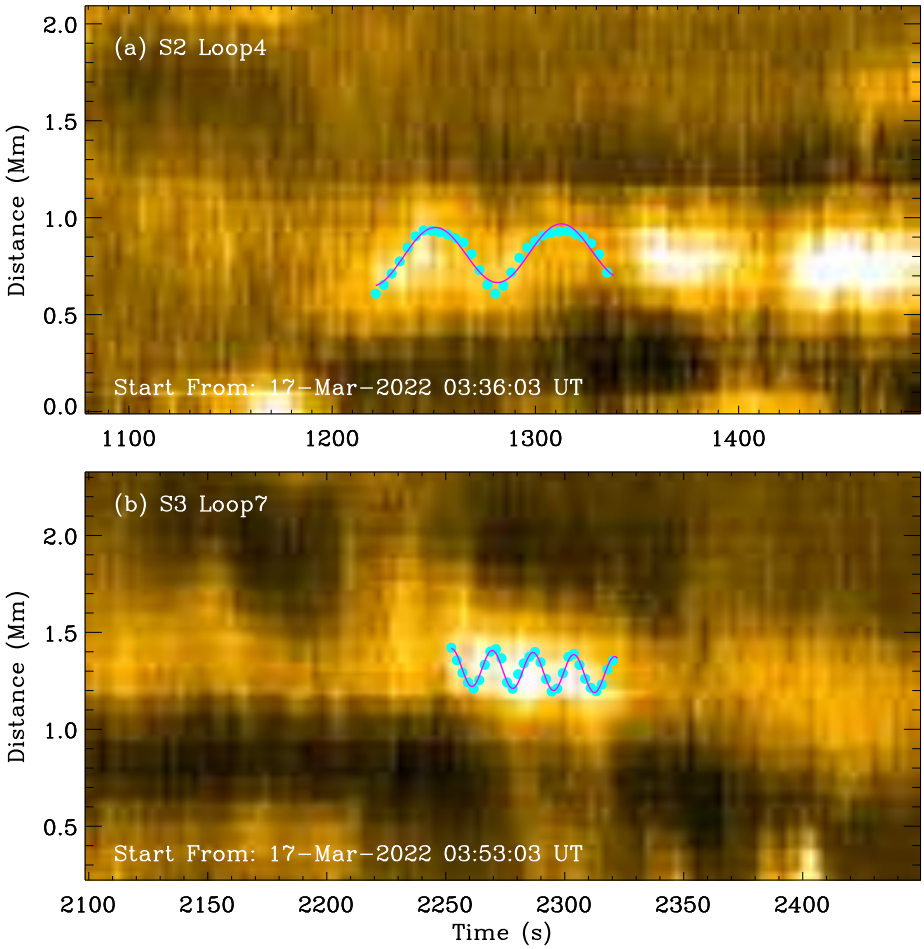

Fig. A3.— Zoomed time-distance diagrams made from slit S3 in region R2 along the oscillating loops 4 (a) and 7 (b). The cyan circles indicate the fitting profile positions of coronal loop oscillations, and the magenta curves represent their best fitting results.

B. Energy estimations

For the large-amplitude decaying oscillation, it was found that the average decaying time is $\tau = 1.79P$, where P is the oscillation period (Section 3.7 in Nechaeva et al. 2019). Based on the damping mechanism, one can construct an equation as follows (cf. Van Doorsselaere et al. 2014; Yuan & Van Doorsselaere 2016a):

$$E(t) = \frac{1}{2}V(\rho_i\ v_m^2 + \frac{b^2}{\mu_0})e^{-2t/\tau}, \tag{B1}$$

where, $E(t)$ represents the total (kinetic+magnetic) energy averaged over oscillation period, V represents the volume of oscillating loops, ρ_i and b are the plasma density and the magnetic field perturbation inside oscillating loops, v_m^2 denotes to the velocity amplitude, μ_0 is the magnetic permittivity of free space, and τ is the decaying time measured for the displacement amplitude.

Then, its derivative $\frac{dE(t)}{dt}$ at $t = 0$ will give us an estimate for the total oscillation energy losses (E_t), such as:

$$E_t = -\frac{V}{\tau}(\rho_i\ v_m^2 + \frac{b^2}{\mu_0}), \tag{B2}$$

Here '-' means that the wave is losing energy. For clarity, we ignore '-' in the next discussion and thus could regard as its contribution to coronal heating.

Assuming that the coronal loop has a constant cross-section (S) (cf. Williams et al. 2021; Gao et al. 2022), and the loop length (L) could also be measured, then we can get $V = SL$. Considering that $c_k = 2L/P$ and $\tau = 1.79P \approx 2P$, the energy flux (E) can be expressed as:

$$E = \frac{E_t}{S} \approx \frac{1}{4}c_k(\rho_i\ v_m^2 + \frac{b^2}{\mu_0}), \tag{B3}$$

Next, assuming that the same damping mechanism with the same damping rate operates in the decayless oscillation, but it is compensated with continuous energy supply from an unknown driver, we can obtain Equation (5) in our work. Therefore, the energy flow in the case of decayless oscillations looks like the following: "unknown driver → standing kink oscillations → rapid damping → plasma heating". Such process continues when an unknown driver is existing, and the decayless oscillation could be detected in the coronal loop.